MEASUREMENTS OF ATMOSPHERIC MUONS USING AMANDA WITH EMPHASIS ON THE PROMPT COMPONENT

by

RAGHUNATH GANUGAPATI

A dissertation submitted in partial fulfillment of the
requirements for the degree of

DOCTOR OF PHILOSOPHY
(PHYSICS)

at the

UNIVERSITY OF WISCONSIN – MADISON

2008

MEASUREMENTS OF ATMOSPHERIC MUONS USING AMANDA WITH EMPHASIS ON THE PROMPT COMPONENT

Raghunath Ganugapati

Under the supervision of Professor Albrecht Karle
At the University of Wisconsin — Madison

The main aim of AMANDA is to detect diffuse extra-terrestrial neutrinos. While atmospheric muons can be easily filtered out atmospheric neutrinos are an irreducible back-ground for diffuse extra-terrestrial neutrino fluxes. At GeV energies the atmospheric neutrino fluxes are dominated by conventional neutrinos. However with increasing energy, the harder "prompt" neutrinos that arise through semi-leptonic decays of hadrons containing heavy quarks, most notably charm, become dominant. Estimates of the magnitude of the prompt atmospheric fluxes differ by almost two orders of magnitude making the significance of evaluating their intensity very important. The main principle in this thesis is that it is possible to overcome the theoretical uncertainty in the magnitude of the prompt neutrino fluxes by deriving their intensity from a measurement of the *down-going prompt muon flux*. An attempt to constrain this flux using this principle was made and analysis of the down-going muon data was performed to constrain the RPQM model of prompt muons by a factor of 3.67 under a strict set of simplifying assumptions.

Albrecht Karle (Adviser)

Acknowledgements

I consider myself immensely fortunate to have pursued my PhD. in physics at the University of Wisconsin-Madison. I feel an immense sense of accomplishment in this intense effort and extended study to attain a PhD, the highest academic degree anyone can earn. To see a high school knack for solving physics and mathematics problems culminate in this great accomplishment is something special. UW-Madison took exceptionally good care of me, so much so, I felt it was a“home away from home”. Closer to home, I would like to thank the Wisconsin Icecube collaboration.

First and foremost, I would like to thank my advisor, Professor Albrecht Karle, for taking me on as a student a few years ago, even though he knew little about me at the time except for the fact that I was that graduate student in engineering at UW-Madison. I would like to thank my mentor the late Bruce Koci and my co-supervisor Professor Bob Morse for help with the IceCube drill modeling work that I did which has been a huge success for the project. I would also like to thank Professor Francis Halzen, Principal Investigator for IceCube who is my role model for modesty and Professor Teresa Montaruli for her stint at advising me. In addition, I would also like to thank Professor David Brown of the Finance department of UW-Madison for advising me on my PhD minor course work in Mathematical Finance and on my stint on Wall St as a “Rocket Scientist”.

I would like to thank all the members of the AMANDA/IceCube collaboration who have interacted with me during the course of this thesis and all the physicists I interacted with at conferences. Notable mentions are Gary Hill, for valuable thesis advice and suggesting that cooking at home was the only way of getting rich in graduate school! Paolo Desiati for convincing me that the idea to investigate prompt muons for a PhD thesis not to be such a horrible one. Mark Krasberg for all the non-physics talk in low times and being one of my close tennis buddies on campus. My fellow graduate students John Kelley (doesn't need a reason to be cheerful!), Jessica Hodges, Jim Braun and Karen Andeen. I would also like to thank Mike Stamatikos, Jodi Cooley, Katherine Rawlins, David Steele and Rellen Hardtke from the older class of graduated students.

With all my heart I thank my parents Lakshmi and Haranath Ganugapati for their encouragement and instilling a knife-edged competitive spirit to prepare me and my brother to gain an admission into the Indian Institute of Technologies and subsequent higher education in the United States. Incidentally my brother is my role model for mathematics, the physics counterpart.

Thanks to Karle's lab and each one of you all for making this possible!

Contents

List of Tables

List of Figures

Chapter 1

Introduction

The Antarctic Muon and Neutrino Detector Array (AMANDA) is designed to detect high energy neutrinos using the three kilometer thick ice cap covering the South Pole. AMANDA in its design consists of a large array of phototubes located under the ice. This array of phototubes embedded in the icecap at depths of 1500 to 2000m captures the Cherenkov radiation from the ultra relativistic charged leptons that are produced when neutrinos undergo charged current interactions with nucleons in the ice.

The main aim of AMANDA is to detect extra-terrestrial neutrinos. The background to the observation of these neutrinos is the flux of atmospheric muons and neutrinos produced in cosmic ray showers in the atmosphere. Atmospheric muons can reach the detector only from above, because the range of muons in earth is only a few kilometers. Atmospheric muons are therefore only downgoing and these can be easily filtered out by using the earth as a filter and looking at upward-moving neutrinos produced in the northern hemisphere. Atmospheric neutrinos can instead reach the detector from all directions. Hence they are an irreducible background for diffuse astrophysical neutrino fluxes. It is very important to evaluate their intensity with reasonable accuracy.

At GeV energies the atmospheric fluxes are dominated by the decays of relatively long-lived particles such as $\pi^{\pm}$ and $K^{\pm}$ mesons. With increasing energy, the probability increases that such particles interact in the atmosphere before decaying. This implies that even a small fraction of short-lived charmed particles can give the dominant contribution to high energy muon and neutrino fluxes. These "prompt" muons and neutrinos arise through semi-leptonic decays of hadrons containing heavy quarks, most notably charm. Estimates of the magnitude of the prompt atmospheric fluxes differ by almost two orders of magnitude making the significance of evaluating their intensity very important.

The main principle in this thesis is that it is possible to overcome the theoretical uncertainty in the magnitude of the prompt neutrino fluxes by deriving their intensity from a measurement of the *down-going prompt muon flux*. The suggestion is based on the observation that due to the charmed particle decay kinematics for the semi-leptonic decays into neutrino and muon fluxes, the prompt muon and neutrino flux are essentially the same at sea level. Importantly, this result is independent of the charm production model. It should be stressed that *down-going prompt muons* and not up-going neutrino induced muons are used to get limits on the prompt neutrino flux. Prompt muons are easy to detect and there are ways of separating them from the conventional muons using different zenith angle and energy spectral shapes.

This analysis of the atmospheric charm component is challenging for the fact that there are no robust simulations for producing atmospheric prompt muons. Further, the limited angular and energy resolutions of AMANDA combined with the lack of availabilty of a model makes life very hard for a researcher.

Studies were also done on the introduction of theoretical models used to calculate the heat transfer and refreezing rates in boreholes in cold ice at the south pole and a comparison of these results with experimental data from the AMANDA holes. The calculations are based on models derived for phase change with a moving boundary layer in cylindrical coordinates. This work improved estimates of fuel consumption and contributed to a better efficiency in the drilling of holes for project IceCube.

Chapter 2

Strategies to optimize the hotwater drilling method for IceCube

During the 1990s 23 holes were drilled to depths ranging from 1000 to 2450 meters at the South Pole to build the AMANDA neutrino telescope. A large hot water drill was used to drill the holes. This technique was chosen because it was the only one conceivable to meet the requirements to produce 60cm diameter holes filled with water. Pioneering efforts to 1000 m depth were successful and allowed the installation of the first optical sensors in polar ice at the South Pole. The drill grew in size as depth and hole diameter requirements increased until it reached a maximum thermal power of 2.2 MW. It became clear that this drill would not be adequate to drill to depths of 2450 meters, required for IceCube. At depths below 2000 meters drilling became slow and inefficient. The next generation IceCube detector would require drilling 80 holes in a five year period. A new enhanced hot water drill (EHWD) with a power of about 5 MW would need to be designed to drill two holes per week. The following study was initiated to optimize the drill design and drilling strategy and confirm relatively rough estimates on fuel consumption. We developed a model that allowed us to calculate a drilling procedure that will result in a hole diameter large enough to ensure successful deployment of detector strings with acceptable fuel requirements. The model suggests drilling and reaming rates based on heat input that will provide an optimum hole diameter profile. The result is a barrel shaped hole that compensates for different freezing rates that are a function of ice temperature and time of exposure to heat. The calculations and predictions are verified from simulations with drill data from the AMANDA holes. The robustness of the calculation is checked by applying perturbations to critical system parameters.

IceCube is a one-cubic-kilometer international high-energy neutrino observatory being installed in the clear deep ice at the South Pole. It will open unexplored bands for astronomy, including the PeV energy region, where the Universe is opaque to high-energy gamma rays originating from beyond the edge of our own galaxy, and where cosmic rays do not carry directional information because of their deflection by magnetic fields. The detector will consist of 80 strings of optical modules placed between 1450 and 2450 meters depth. This depth range takes advantage of the clear ice below the bubbly ice region and avoids the shear layer between the bottom of the ice and the detector. The holes will have a diameter of approximately 60 cm to support the installation of the optical module strings, which are 43 cm in diameter. The additional size is required to compensate for freezing that takes place on the hole walls after drilling and during deployment. Hot water drills operate by pumping water that has been heated under high pressure to a drill head where the hot water jet is used to melt the ice. In impermeable ice, the hole is filled with water, which is recycled to the surface by a submersible pump. The water is then reheated and pumped through the drill head to melt more ice. Approximately 8% of the ice volume must be replaced by water from the surface to make up for the volume lost in the phase change. Before the AMANDA project these drills were generally portable and limited to less than 1500 meters in depth and to smaller diameters. The cold $-50°C$ ice at Sthe South Pole, depth requirement of 2400m and hole diameter of 60 cm required a much larger drill. The drill used for AMANDA evolved over the life of the project and grew from 1.6 to 2.2 MW maximum heat input. The drill was pressure limited to 1000 psi operating pressure, which limited flow as lengths of hose were added. At depths beyond 2000 meters the drill became increasingly inefficient. Fuel consumption per hole was over 10000 gallons and the time required to drill a 2400 meter hole was well over 100 hours, in one case more than 150 hours. Neither of these figures was acceptable for the 80 holes required for IceCube. A new drill design was proposed that would provide a constant heat input of about 5 MW over the entire drilling depth. A larger hose was needed to accommodate the higher flow and the hose was to be housed on a single large reel. Single point power generation, with heat scavenging, have replaced ancient generators and diesel driven pumps to improve efficiency. In addition the entire drill heating and pumping plant have been placed in mobile drilling structures that reduce set up and build down time. The goal is to drill up to 18 holes per year, completing 2 holes per week. The 40 hour drilling time per hole drives the heat input. Since the drills have all been equipped with calipers and navigation packages, it is possible to create a map of the hole including a diameter vs depth curve. These measurements and curves are required to assure the hole diameter remains large enough to permit the deployment of the optical modules over a 30-hour period after drilling ceases.

Crude models were constructed during the AMANDA project to predict the amount of freezing that would occur during this period. This paper is an introduction to the theoretical models used to calculate the heat transfer and refreezing rates in boreholes in cold ice and to compare the results with experimental data from the AMANDA holes. The calculations are based on models derived for phase change with a moving boundary layer in cylindrical coordinates.

2.1 Description of the thermal process

A large hot water drilling system consists typically of the following main components.

- High-pressure pumps to pump the water to the drill head.
- Heaters to heat the water to near boiling.
- Drill hose to deliver the water to the drill.
- Drill head and nozzle to direct water to the front to warm and melt ice.
- A return submersible pump to recycle cold water from the bore-hole.

The surface components consist of high-pressure pumps and a heating plant. Heat losses from this part of the system are low compared of the total heat budget in large drill systems because the hoses are well insulated. The hose hangs vertically in the hole, which is filled with water below a depth of 50 m. A parcel of water moving through the hose loses heat to the surrounding water through conduction across the hose wall and convection to the surrounding water, which is moving slowly up the hole. The advective term is ignored in these calculations. It is desirable to move the

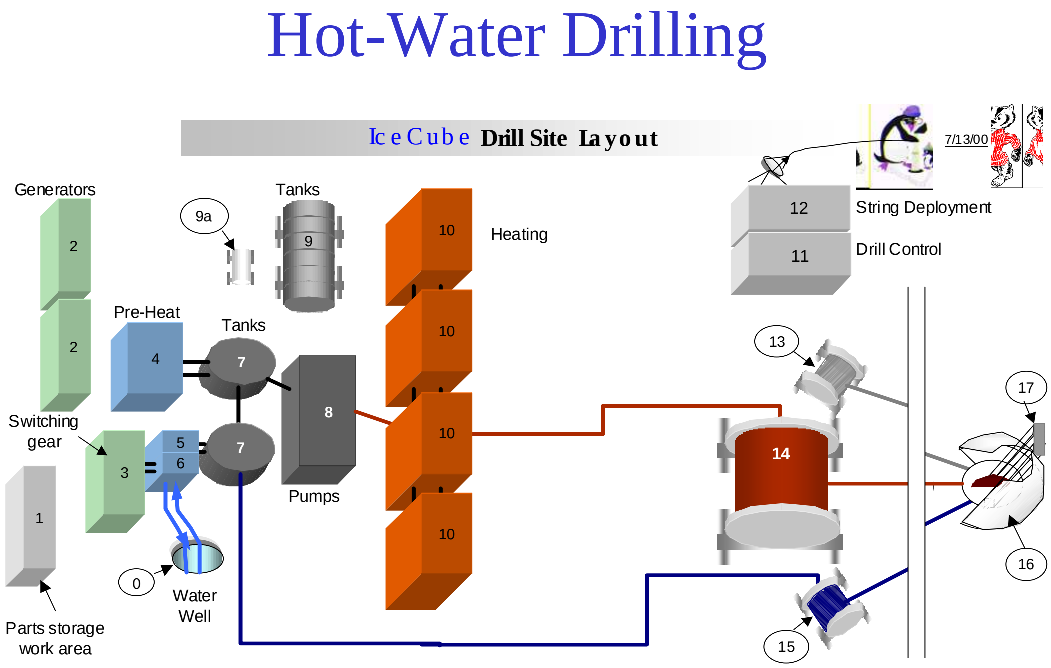

Figure 2.1: The figure describes the schematic view of the IceCube Enhanced Hot Water Drill (EHWD) at the surface.

water through the hose as rapidly as possible to keep the residence time in the hose to a minimum. The amount of heat available at the nozzle drops exponentially with a decay length λ of the hose where the heat available has fallen to half of that available at the surface. The decay length depends on the conductivity of the hose material, the hose wall thickness and the velocity of fluid through the hose. Heat lost through the hose helps keep the hole from refreezing. Later we will discuss how the decay length influences drilling and reaming efficiency.

The hot water drill head consists of a massive steel pipe to keep the drill plumb, and a housing for the electronics and navigation package. A nozzle is designed to accelerate the speed of the water while keeping the flow intact to create turbulence ahead of the drill. In cold ice as at South Pole the ice must first be warmed before

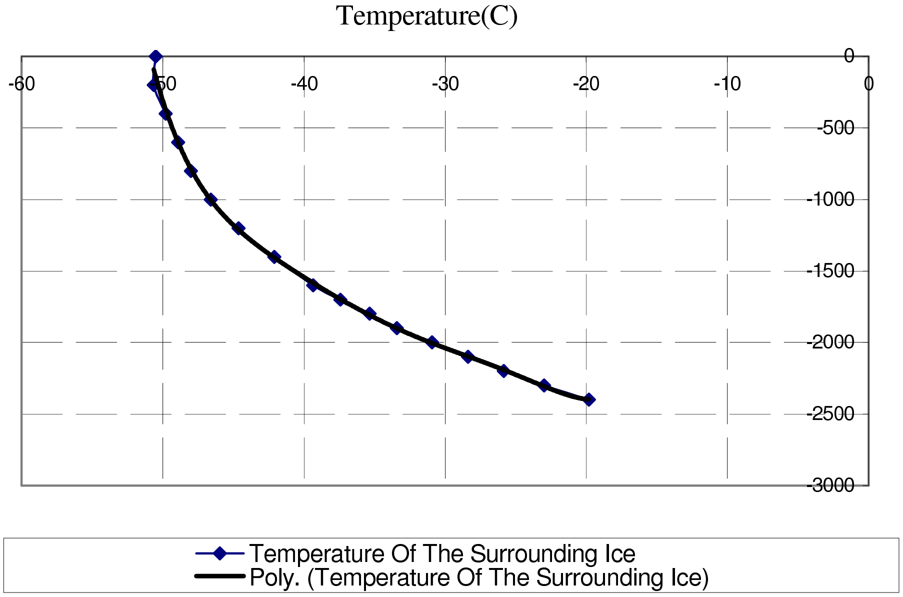

Figure 2.2: Depth dependnce of the temperature of South Pole Ice.

it can be melted. This can limit drilling speed if the narrow portion of the drill is short or the velocity at the nozzle is low. A temperature profile of the ice at the South Pole is shown in figure 2.2. The heat provided by the injected hot water of about 800 liters/min is not dissipated immediately. Energy remains in the form of hot water that continues to warm and melt the surrounding ice. Some of the energy is conducted into the surrounding ice. The result is a long plume of warm water that gradually melts the hole wall to a larger diameter with time. With large hot water drills such as the AMANDA or IceCube drill this plume can extend more than 100 meters behind the drill.

As the return flow drifts back up, the cold water column is slightly heated by losses from the hose. These losses slow the refreezing rate. The effects will be discussed in a later section. Water at the top of the hole having a temperature of $2°C$ is recycled using a submersible pump.

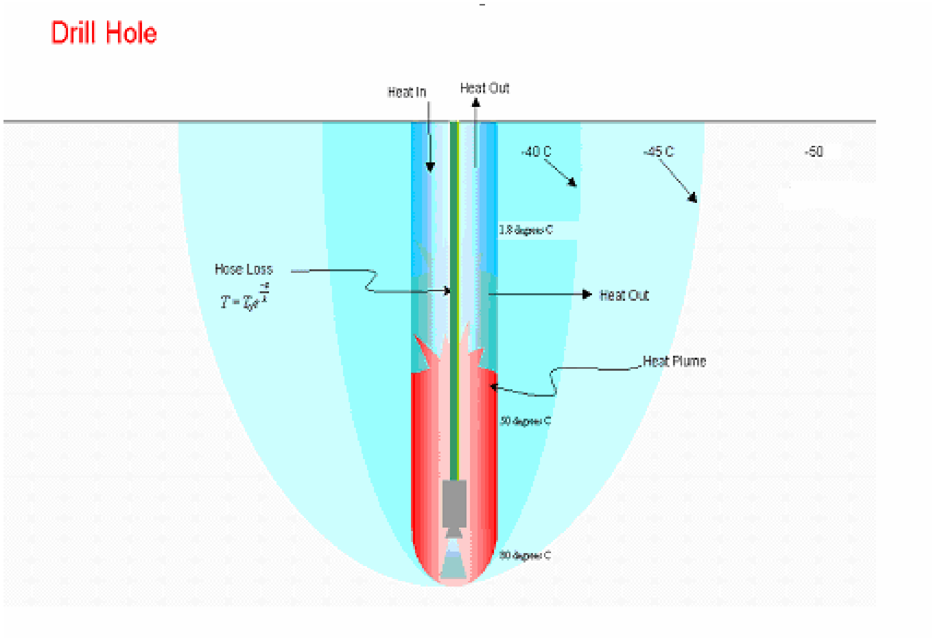

Figure 2.3: Schematic view of the hotwater drilling method.

At the surface water is pumped through heaters into the high-pressure hose, which transports the energy into the borehole where it is used for melting the ice. The heat input to the borehole is determined from the flux and temperature of pumped water. The hose at the surface is usually well insulated and the water typically loses only 2-3 °C from the point on the surface where it is pumped until it reaches the top of the borehole.

A hot water packet takes several minutes travel down the hose to the drill tip, so an imperfectly insulated hose conducts heat to the surrounding borehole which is typically filled with cold water. The hose and cable tension is monitored to ensure that the drill tip does not touch the bottom of the hole. A parcel of fluid traveling down the hose can be said to lose heat only through the walls of the hose, since the temperature gradients along the direction of flow are negligible as compared to the radial gradients.

These hose losses slow down the process of refreezing that occurs at the top of the hole and cannot be regarded as a waste. Because of the exponential decay of temperature and consequently the power available, it is important to maximize the flow within the pressure capability of the hose. For the EHWD the thermal conductivity of the hose is 0.4W/m-K [2] and the flow rate is 200 gallons/minute and thus λ is around 8000m. There would also be an advective term, which comes from the conductivity of the water that fills the hole. In the problem we shall neglect advective heat transfer, which would fluctuate as the hole size changes. In the past, water was heated to 90°C, losing heat as it travels from the heating plant to the surface of the hole. The calculations that follow were done with a surface temperature of 88°C, which can be obtained by suitably insulating the hose from the heaters to the hole opening without much heat lost into the surrounding atmosphere.

2.2 Methodology and Assumptions

Symmetry allows for an assumption of azimuthal independence. We will simplify the problem to the one along the radial direction alone because the longitudinal gradients are negligible. As the heat is exchanged across the ice-water boundary refreezing will occur. The moving boundary of the phase change interface presents special difficulties for numerical procedures, since the position of the boundary is dependent upon a varying temperature field in ice. The boundary condition would be that the temperature of the ice water interface is always at 0°C. At each time step the change in radius is calculated from the amount of heat that enters the system in the form of hose losses and the amount of left over heat energy that goes from the hot water that is left after the initial melting has occurred. The heat left decays exponentially and for purposes of our calculation, we assume that this heat continues to melt the ice for a period of four hours after which it goes down to about 2C when it becomes cold enough that it can no longer melt ice. However, in this section we will briefly look at the underlying equations. The problem may be formulated in cylindrical co-ordinates with the z-axis directed downward from the surface along the axis of the hole. The system is azimuthally symmetric. We will simplify the problem to one along the radial direction alone because the longitudinal gradients are negligible.

2.3 Description of the model and assumptions

Here we describe a list of the model assumptions in the calculation:

a) The method used to solve the heat transfer differential equation is a numerical finite difference method. For this purpose, we modeled the problem with a space mesh where the grid element was 0.15 cm wide (1% of the initial radius). We used 1300 elements to span a total area of $3.6\,m^2$ at each depth. The number of elements in the grid is chosen in such a way that the solution to the problem converges at each depth in a reasonable time and with sufficient precision. The number of grid points chosen was increased until the result didn't change significantly with increasing resolution.

b) The time resolution for each time step was taken as 0.0001 times the characteristic time of the system, which is the total borehole closure time (100 hours). Each time the size of the hole changed, the number of grid points inside the boundary were suitably adjusted, allowing us to locate the point on the ice-water interface.

c) Total heatflow is 200 gal/min of water with a temperature of 88°C at the top of the borehole. This corresponds to a total power of 4.65MW at the top of the hole.

d) The circulated water loses around 40% of the heat before it travels from the nozzle to the widest point of the drill hole (15m above the drill head). This heat is available for initial melting and for constructing a sufficient diameter hole for the drill to fit. This process takes 1-2 minutes and is assumed to be non-heat conducting with regards to the surrounding ice. The temperature to which the water cools during this instantaneous conduction is given by 54exp(-z/λ), where z is the depth and λ is the decay length of the hose.

e) Once the initial melting described above is complete, the hot water remains inside the hole and continues to increase the diameter of the hole, as some of the heat is lost into its surroundings. This process has been modeled as a typical steady-state heat conduction problem with a 4-hour duration and an exponential decay function, where half of the heat decays in the first hour.

f) We modeled the down-hole path as segments of length 100m at constant temperature. The conditions inside each slice are assumed to be non-varying and the heat transfer equations are solved inside the mesh surrounding it. Once all the calculations are done for one slice we move onto the next slice and so on.

g) A final target diameter at 45cm in each of the 100m slices at the end of operation was set.

h) The thermal properties of ice (specific heat and freezing point) are assumed to be constant throughout the hole.

i) We obtained the hose losses by dividing the total heat available at any depth by the λ of the hose. We neglected the conductivity of the water, so all thermal conductivity is assumed to come from the hose alone. By neglecting the advective heat transfer, we may have overestimated the hose losses and underestimated the heat

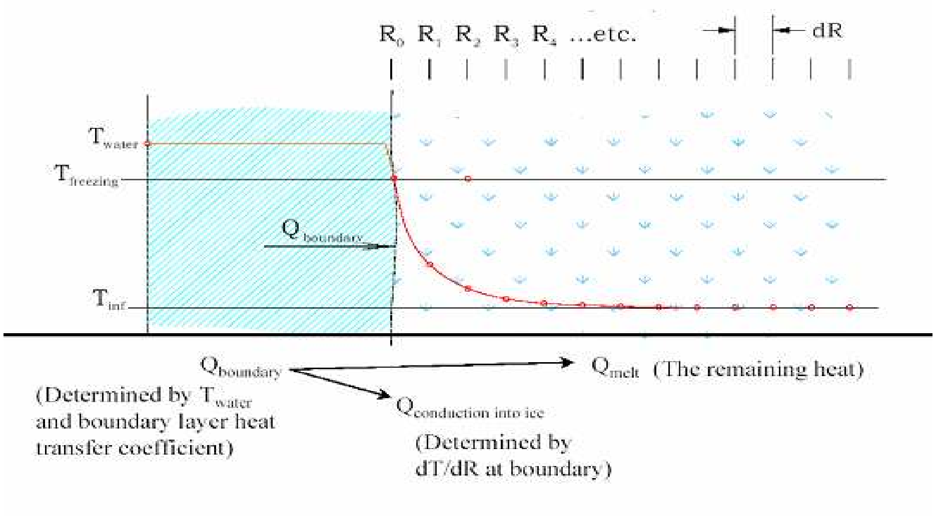

Figure 2.4: The figure illustrates the heat transfer procedure that asymptotically approaches the far-field ice temperature.

available at the bottom of the hole but all these corrections can be neglected to first order.

j) We model the reams as an instantaneous process in which no heat is conducted into the surrounding ice and it is entirely used for melting the ice on the borehole walls.

2.4 Optimal drilling algorithm

The drilling strategy is optimized to obtain a hole of constant diameter at some specified time of typically 35 hours after drilling is completed. The minimum amount of time that we spend inside the hole subjected to constraints like the target uniform diameter after deployment being 45 cm and the drill fitting through can be accomplished by a simplex minimizer however it can be observed that the solutions to the problem exhibit monotonic nature and thus we can find the optimum just by moving in one direction. The final time step to obtain optimum solution is in turn dependent on the solutions in each of the slices so there is a need for a first guess solution. We start out at a high drill speed of 200m/hr and a ream speed of 450m/hr respectively inside the slice. We calculate the initial diameter that we obtain from the cooling of water from the nozzle to the drill head. If we don't get sufficient size of the hole (initial diameter) for the drill to fit through then we reduce the drill speed by 5m/hr until the condition of the drill passing through is met. There is a maximum of the drill speed that we use for our optimization. Once this condition is met we calculate the position of the ice-water boundary at a time t, the initial guess on total time spent inside the hole plus the estimated deployment time. If the diameter of the hole is less than the target diameter of 45cm then we reduce the ream speed in steps of 10m/hr and check if we reach the target diameter at which point we stop and move onto the next slice. Once the minimum limit on ream speed (180m/hr) is reached without the target diameter getting to 45 cm, we reduce the drill speed from the maximum limit obtained for the drill to fit through in steps of 5m/hr till we get the required target diameter. Once the required target diameter is established we record the values of the drill speed and the ream speed used for accomplishing the required target diameter and calculate the time spent by the drill head in this slice during the drilling and the reaming operations. Then we move on to the next 100metre slice, the drilling operation in this slice is delayed by a factor of time that we spent in the previous slices drilling, in other words it takes time for the drill to get here so we subtract the time we spent till we get to this slice from our initial guess on total time. This analysis is repeated in slices of 100 metres until we get to the bottom of the hole. By summing up the times spent drilling and reaming in each of these slices we get the total time spent inside the hole. This should for iterative purposes be close to our initial guess of 50 hours. If this is lesser (which is usually the case, considering that we start out with a larger value than what we think our solution is going to be) then we reduce the initial guess (50 hours) in steps of 1 hour and repeat the entire procedure described in this section till the iteration is established. Thus the drill speed, ream speed and other parameters at each depth that satisfy all these conditions are the solutions to our optimization problem. At these parameter values we get a uniform hole of 45cm in diameter at all depths and this also minimizes the total time spent by the drill inside the hole.

2.5 Results

A baseline model assumes the most likely values for the parameters encountered in the actual field operation. The results of the optimization process are shown in the following figures. Figure 2.5 illustrates the optimal refreeze process. While the hole is drilled at different times and the refreeze rates differ with depth they reach an identical diameter at a predefined target time. This is the time theoretically available for the deployment team to deploy the string. After this time the hole would be too small and the string would get stuck and freeze in prematurely. Obviously some contingency time needs to be taken into account to ensure a safe deployment process.

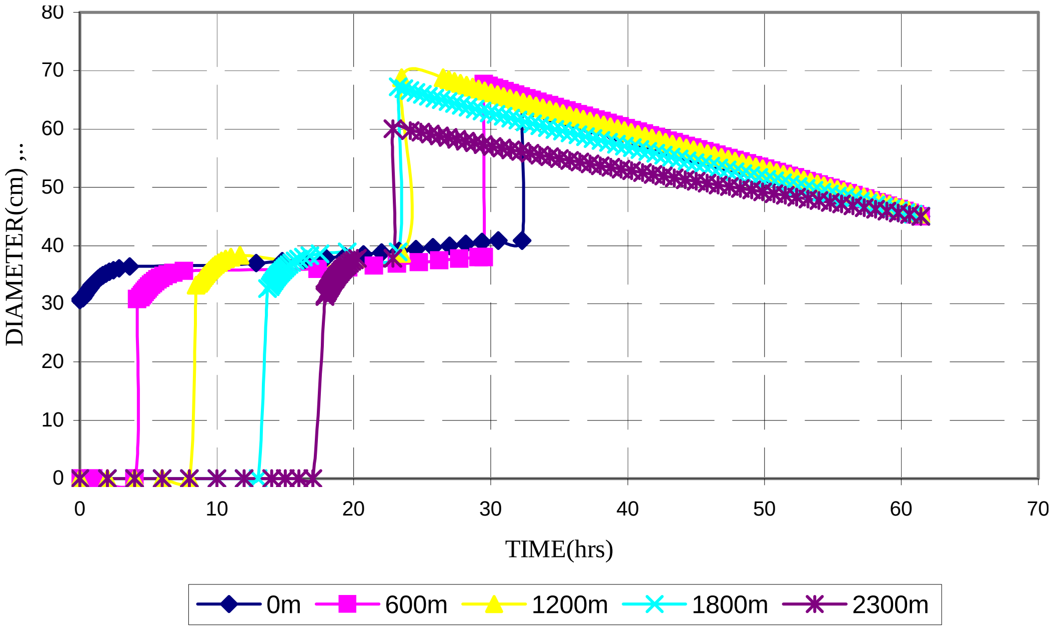

Figure 2.5: The hole diameter as a function of time for a range of depths. The drill strategy delivers a hole of uniform diameter at a required time of 30 hours after the drilling is completed.

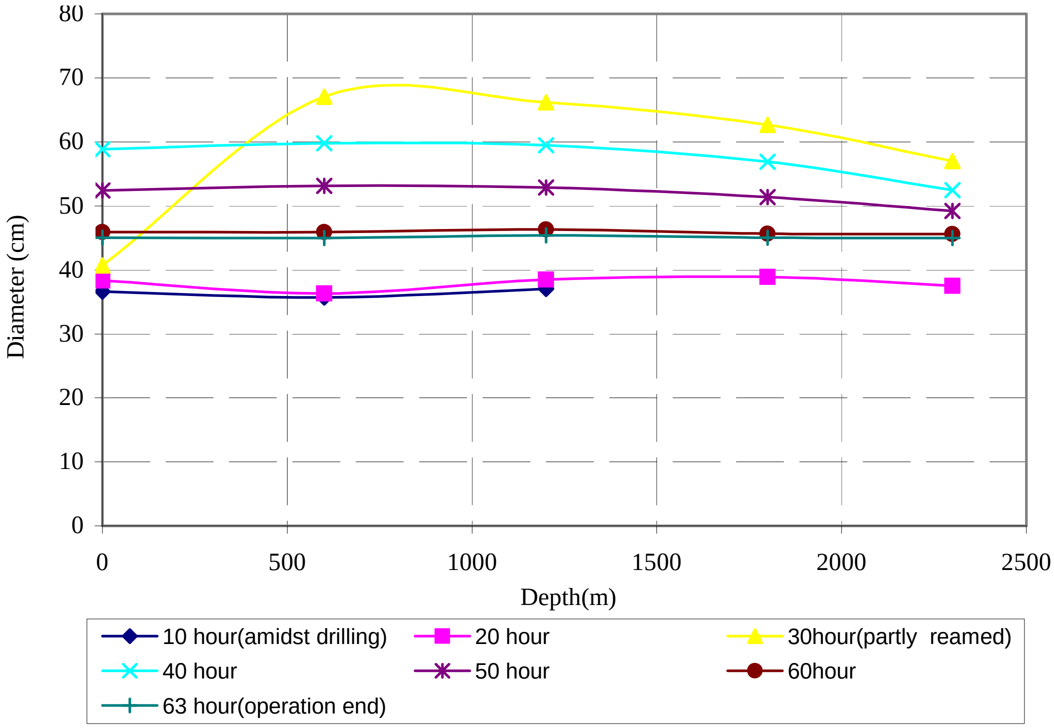

Figure 2.6: This figure summarizes the evolution of the hole size.

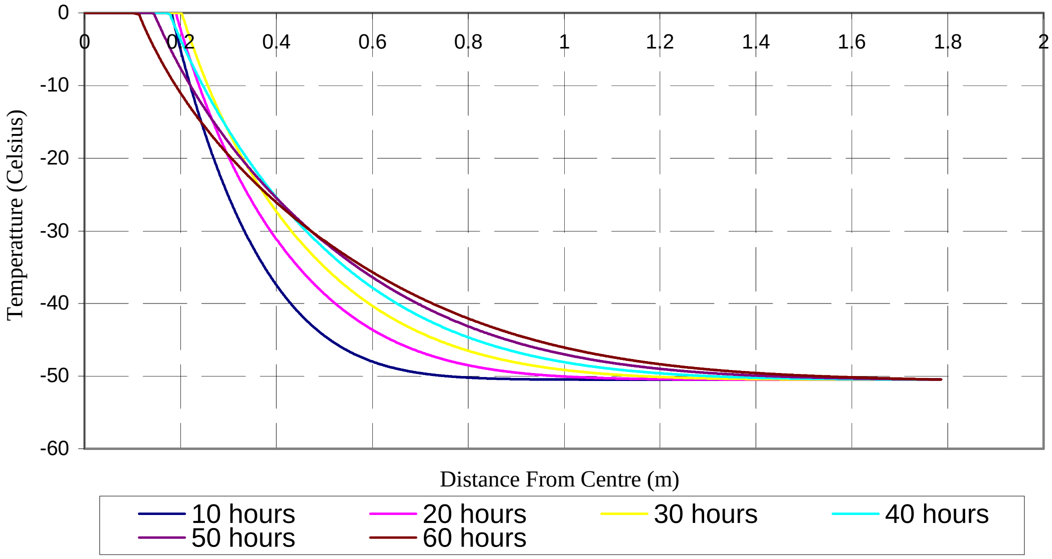

Figure 2.7: This figure summarizes the evolution of the hole diameter as a function of time. The drill strategy delivers a hole of uniform diameter at a required time of 30 hours after the drilling is completed.

2.6 Robustness of Predictions

The above analysis assumes that the inputs used are known accurately. However, the inputs could generally vary due to fluctuations during the drilling operation or simply because they haven't been accurately determined. So we performed another analysis in which we allowed a perturbation on one input at a time and checked the results against our original overall drilling strategy, paying special attention to the total time we spend inside the hole and our fuel estimates. The decay length, power available at surface, deployment time and desired target diameter are varied and a range of outputs corresponding to optimal strategy are quoted in tabular forms.

	λ = 5000m	**λ = 8000m**
Heat (Surface to 800m) (MW)	5.0	2.2
Heat In (at 2000m) (MW)	5.0	1.9
Heat Out (at 2000m) (MW)	4.0	1.6
Drill Rate (at 2000m) (meters/minute)	1.5 – 2.0	0.5
Flow Rate (at 2000m) (gallons/minute)	200	85
Fuel Consumption (gallons/hour)	200	85
Weight (pounds)	400000	250000
Set-up Time (days)	18 – 25	35 – 42
Fuel (gallons/hole)	6000 – 7000	10000 – 12000

Table 2.1: The input parameters that go into the old AMANDA drill (λ = 5000m) and the new IceCube drill (λ = 8000m) are compared.

	λ= 5000m	λ= 8000m	λ= 11000m
Drill Time (hrs)	19.28	19.06	21.17
Ream Time (hrs)	10.67	12.36	13.00
Total Time (hrs)	30.00	31.42	32.55
Total Energy Deposited (GJ)	510	538	549
Energy lost to Surroundings (GJ)	358	386	397
Energy Ratio	0.948	1.00	1.02
Drill Fuel (gal)	3856	3812	4234
Total Fuel (gal)	6000	6284	6550

Table 2.2: The outputs for the optimum strategy and consequently the fuel consumption are quoted by varying the thermal conductivity of the hose λ

	20hr deploy	**25hr deploy**	**35hr deploy**	**40hr deploy**
Drill Time (hrs)	17.96	17.96	20.52	23.53
Ream Time (hrs)	9.50	11.29	13.16	13.14
Total Time (hrs)	27.47	29.25	33.68	36.68
Total Energy Deposited (GJ)	465.3	495.6	570.48	621
Energy lost to Surroundings (GJ)	313.3	343.6	418.48	469
Energy Ratio	0.864	0.921	1.06	1.154
Drill Fuel (gallons)	3592	3592	4104	4706
Total Fuel (gallons)	5494	5850	6736	7336

Table 2.3: The output parameters corresponding to the optimum strategy and consequently the fuel consumption are quoted by varying the deployment time.

	5 % powercut	**10 %** powercut	**15 %** powercut	**20 %** powercut
Drill Time (hrs)	20.93	23.6	26.9	31.25
Ream Time (hrs)	12.90	13.18	13.40	13.63
Total Time (hrs)	33.83	36.78	40.36	44.89
Total Energy Deposited (GJ)	544.3	560	580.6	608.2
Energy lost to Surroundings (GJ)	392.3	408	428.6	456.2
Energy Ratio	1.01	1.04	1.077	1.128
Drill Fuel (gallons)	3977	4248	4573	5000
Total Fuel (gallons)	6437.2	6620	6860	7182.4

Table 2.4: The output parameters corresponding to the optimum strategy and consequently the fuel consumption are quoted by cutting down the power available.

	Diameter=45cm	**Diameter=50cm**
Drill Time (hrs)	19.06	22.24
Ream Time (hrs)	12.36	13.29
Total Time (hrs)	31.42	35.53
Total Energy Deposited (GJ)	538	601.8
Energy lost to Surroundings (GJ)	386	424.3
Energy Ratio	1.01	1.12
Drill Fuel (gallons)	3812	4448
Total Fuel (gallons)	6284	7106

Table 2.5: The output parameters corresponding to the optimum strategy and consequently the fuel consumption are quoted by varying the desired target diameter.

2.7 Conclusions and Summary

A fundamental analysis of the available drill data and a heat transfer simulation was performed. Further a thermodynamic analysis of the process of drilling and refreeze and compared our results with existing data. This provided a better prediction of the refreeze rates and an optimal strategy for efficiently drilling uniform holes. We also infer that it is always better strategy to put energy into the ice as late as possible to prevent it from refreezing; in other words drill fast and ream slow. This is because when we put in heat energy late we are fighting less steep temperature gradients in the surrounding ice. In order to make full use of the analysis we propose a more regulated system called the smart drill. In this system the computer would regulate the drill speed in such a way that the borehole diameter is uniform and of the size as predicted by an optimized freeze back prediction. Studying the system perturbations on a one at a time basis gave us valuable insights into the development of such a system. A significant improvement in hole quality and fuel consumption will be to the benefit of the proposed IceCube project. The modifications suggested in this analysis contributed to a significant reduction of the fuel consumption for the IceCube holes that have been drilled to date (40 holes as of 2008).

Chapter 3

Measuring the Prompt Atmospheric Neutrino Flux with Downgoing Muons in AMANDA-II

3.1 AMANDA Detector

The AMANDA-II detector, Antarctic Muon and Neutrino Detesctor Array, is located at the South Pole. It consists of a total of 677 optical modules. Each module comprises of photomultiplier tube and the hardware inside a glass pressure sphere. These optical modules are attached to 19 strings frozen into the ice, these sensors are deployed across a range of depths from 1500m to 2000m in a cylinder of 100 m radius. These modules detect Cherenkov light from secondary charged particles that are produced from the interaction of a neutrino with ice. AMANDA is integrated into IceCube detector which is still under construction. IceCube will consist of 70-80 detector strings, each with 60 optical modules. Currently 40 strings are deployed and are taking data.

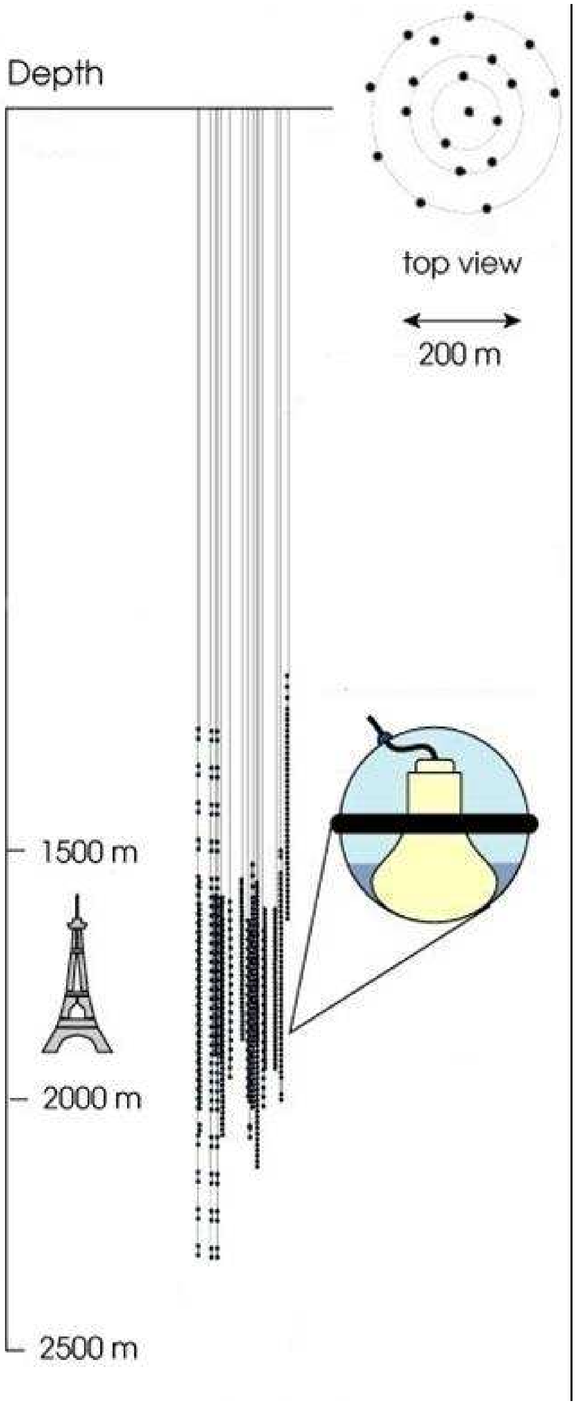

Figure 3.1: The figure shows the layout of the AMANDA detector. The top view shows 19 strings that were deployed. AMANDA detector is roughly 200m wide and 500m long

Detectors like AMANDA-II are sensitive to an energy region in which contributions from prompt charm decays in cosmic ray showers cannot be neglected and may constitute an interesting signal as well as a significant background depending on the nature of the analysis. In searches for diffuse fluxes of astrophysical neutrinos the signal must be separated at high energies from the background of atmospheric neutrinos. Atmospheric muons can reach the detector only from above (downgoing through the earth) because the range of muons in earth is only a few kilometers. Atmospheric muons are therefore only downgoing. Their flux is typically so high that the region of sky accessible to even very deep neutrino telescopes is only the hemisphere below the horizon. Atmospheric neutrinos can instead reach the detector from all directions. Hence they are an irreducible background for diffuse astrophysical neutrino fluxes. It is therefore, very important to evaluate their intensity with reasonable accuracy.

3.2 Conventional and Prompt Atmospheric Neutrinos

When cosmic rays interact with the nuclei in the atmosphere there are two types of particles that are produced that could decay subsequently to give the muon and neutrino fluxes observed. Once these particles are produced in the atmosphere there is a competition between interaction and decay. The critical energy at which the interaction and decay lengths become equal is defined as

$$\epsilon_{\text{crit}} = \frac{mc^2}{c\tau} h_o \tag{3.1}$$

where mc^2 is the particle's rest energy, τ the mean life time and the scale constant h_o that comes from the assumption of an isothermal atmosphere [36].

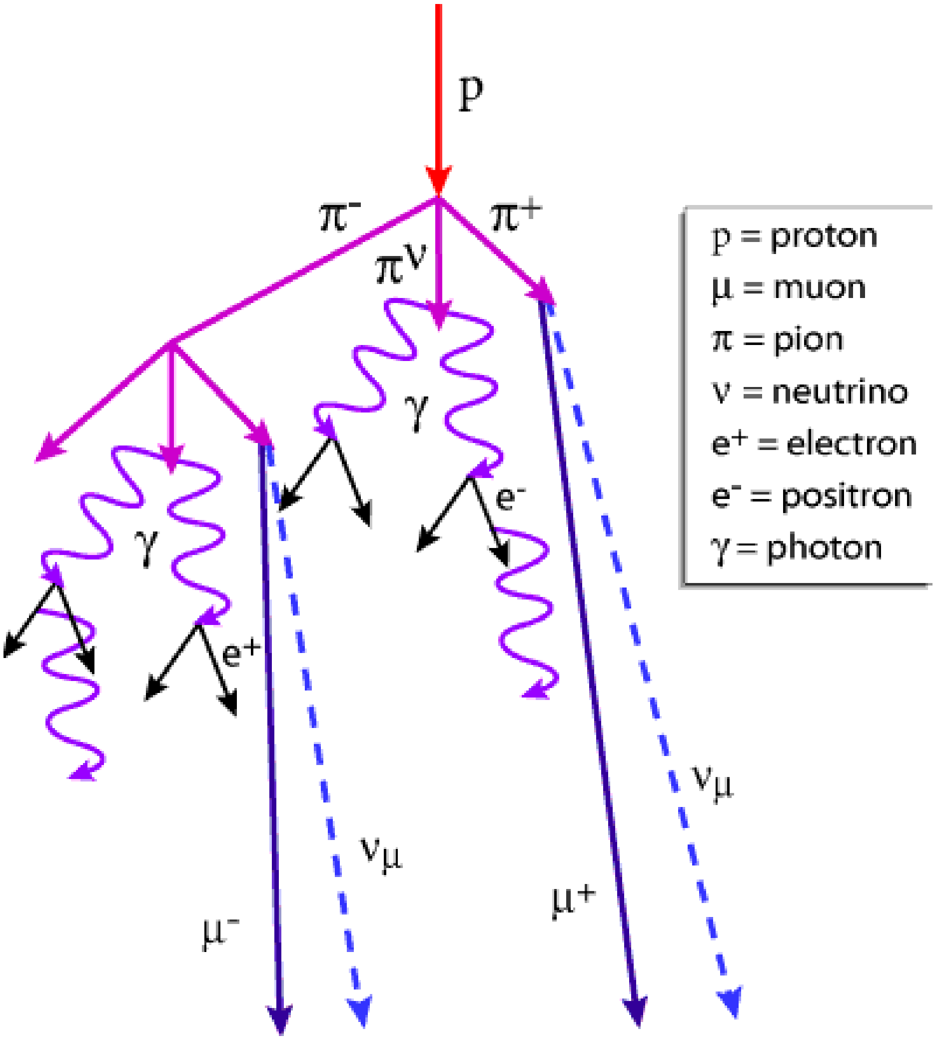

Figure 3.2: The figure schemtically shows the interaction of the primary cosmic ray proton with the atmosphere and the formation of several particles as the shower evolves. (Image credit: Milagro)

Particle	ϵ_{crit} (GeV)
$\mu^{\pm}$	1.0
$\pi^{\pm}$	115
$\mathrm{K}^{\pm}$	850
$\mathrm{D}^{\pm}$	3.8×10^{7}
D^{0},$\bar{\mathrm{D}}^{0}$	9.6×10^{7}
$\mathrm{D}_{\mathrm{s}}^{\pm}$	8.5×10^{7}
Λ_{c}^{+}	2.4×10^{8}

Table 3.1: Critical energy for different particles.

Table 3.1 lists the critical energy of parent particles of muons and neutrinos. These particles could decay and contribute to the atmospheric muon and neutrino fluxes. As can be seen, this critical energy is very high for charmed particles so charmed particles decay readily and muons from them are called "prompt" muons. Above this energy the parent particle is likely to interact or be slowed down before decaying into a neutrino and muon. Since prompt muons are produced readily they follow a $\Phi \propto \mathrm{E}^{-2.7}$ spectrum resembling the primary cosmic ray spectrum. The $\pi^{\pm}$ and $K^{\pm}$ mesons decay into conventional neutrinos only if they dont interact in the atmosphere. If interaction takes place they disappear in the atmosphere and hence the spectra of conventional neutrinos follows a $\Phi \propto \mathrm{E}^{-3.7}$ spectrum.

3.3 Constraining the Prompt Neutrino Flux with the Down-going Muon Flux

With increasing energy prompt neutrinos become the biggest source of uncertainty in predictions of the atmospheric neutrino flux. The DPMJET-II.55 is the only model available for simulating prompt muons and it uses a Naumov RQPM model

[38]. Details of the model are discussed in the next section. As can be seen in figure 3.3 the crossover between conventional neutrinos and the Naumov RQPM model of charm is between 40 and 200 TeV. The level of prompt neutrinos is a potential problem which would limit the search for diffuse astrophysical neutrinos at energies above a few tens of TeV. The suggestion in this thesis is based on the observation that due to the charmed particle decay kinematics for semi-leptonic decays into muon and neutrino fluxes these fluxes are essentially the same at sea level. This result is independent of the charm production model and hence a constraint on a prompt muon flux is equivalent to a constraint on the prompt neutrino flux [31]. There are ways of separating the prompt muons from the conventional muons in underwater or under-ice detectors, such as the different zenith angle dependence, the different depth dependence at a given zenith angle, and the different spectral shape at a given depth and zenith angle [31].

3.4 Prompt Atmospheric Neutrino Models

The prompt atmospheric neutrino fluxes are uncertain by more than 2 orders of magnitude. This is because ground-based particle accelerators cannot reach the energies at which particles are produced in the atmosphere. The uncertainty stems from the need to extrapolate accelerator data to the high energies probed and the uncertainities in parameters that go into each model: the primary spectral index, the critical energy for decay and the Interaction and decay lengths can also play a role.

The **Naumov RQPM** (Recombination Quark Parton Model) [38, 39] tested in this thesis is a phenomenological non-perturbative model that takes into account the contribution of intrinsic charm to the production process. It is assumed that $c\bar{c}$ pairs

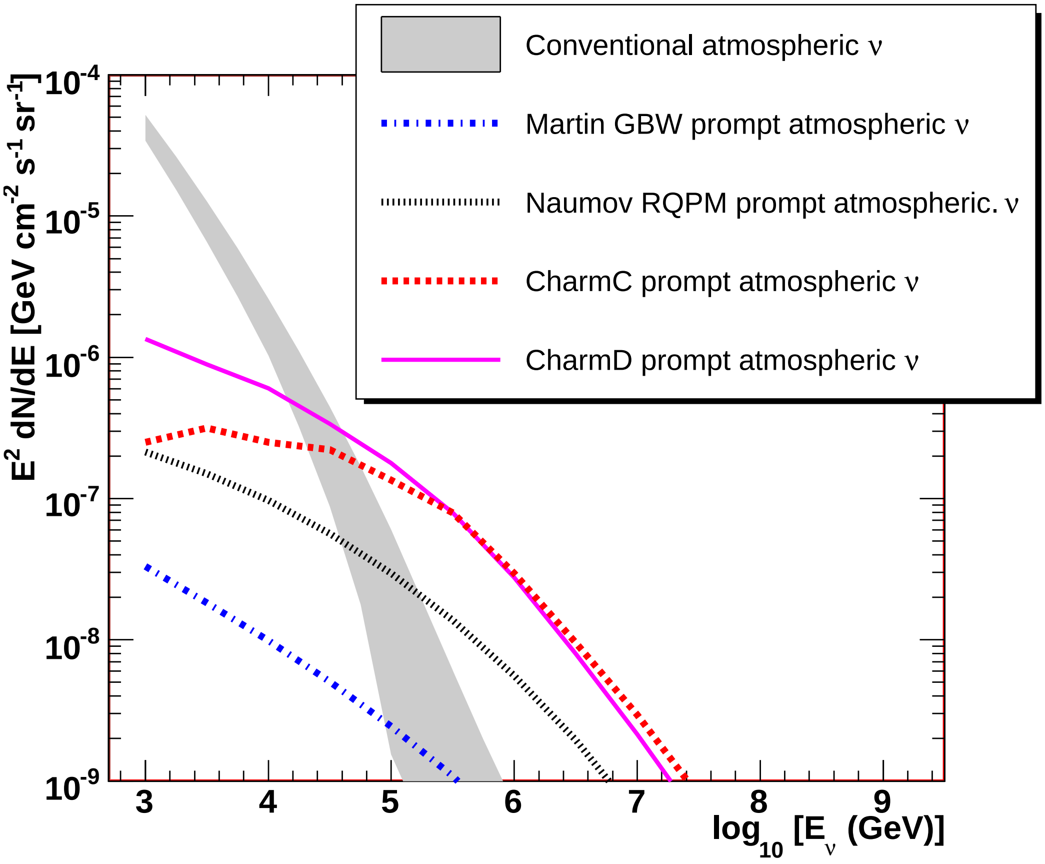

Figure 3.3: Prompt atmospheric neutrinos are predicted to follow a harder spectrum than conventional atmospheric neutrinos. The flux of prompt atmospheric neutrinos is highly uncertain and predictions range over several orders of magnitude. Image Credit: Jessica Hodges

are coupled to a number of constituents in the projectile hadron [40]. The production of mesons such as $\pi^{\pm}$ and $K^{\pm}$ in the fragmentation region of proton collisions proceeds via quark recombination. The evidence for the recombination mechanism comes from the observation that the longitudinal momentum distribution of the pions in the fragmentation region of an incident proton is very similar to the distribution of the valence quarks that they share in the proton, as is revealed in deep inelastic scattering experiments [44].

3.5 Charm in CORSIKA

CORSIKA is a simulation software package to simulate air showers induced by primary cosmic rays. The program produces large amounts of data of all the secondary particles (electromagnetic particles, muons and hadrons). An interaction model is used to describe the physics of the interactions between cosmic rays and the atmosphere. The older DPMJET interaction model of CORSIKA produced charmed particles but they were never allowed to decay so prompt muons could not be simulated. The energy spectra for prompt muons had to be taken at the surface of the earth from empirical parametrizations [33] and muons of multiplicity one were simulated because of lack of prior knowledge of prompt muon multiplicities. In the DPMJET-II-55 framework [20] charmed particles were treated and hence prompt muons produced subsequently were tagged through a generation counter based on their parent [16]. For demonstration purposes the case of first interaction alone was isolated from multiple interactions in the atmosphere. The plots at the surface of the earth for the energy spectra and lateral separation from shower axis are shown in figures 3.4 and 3.5 respectively. Figure 3.4 shows that there is not much discrimination power between prompt muons and conventional muons when lateral distributions are compared using the DPMJET-II.55 model. This contradicts the hypothesis that prompt muons are single muons as was previously hypothesized when we didn't have a prompt muon simulation. DPMJET-II.55 provided us with a reference model for prompt muons and proved to us that any strategy to separate prompt muons from conventional muons has to be focused on using the flatter energy and zenith dependence of prompt muons; if one were to identify these signal events on top of the background events from conventional muons.

An important part of being able to do a prompt muon analysis using the DPMJET-II.55 interaction model of CORSIKA is being able to identify them. If one is interested in muons which come from a decay of ordinary mesons generated in the first interaction, CORSIKA is run and the particle file is scanned for those muons which come from the first interaction by looking for the generation counter. In CORSIKA the generation counter is available that tracks the parents of the particles produced. For instance, for the decays from pions the counter is augmented by 51, for charmed particles it is 31 to get a discrimination against all other muons. The tagging could also be used to identify the muons from first interaction using the number on the generation counter during the production. If an event contains one or more muons that have their parent as a charmed particle we identify them as prompt muons. A need to tag the prompt muon events was accomplished this way.

An important part of being able to do a prompt muon analysis using the DPMJET-II.55 interaction model of CORSIKA is being able to identify them. If one is intrested in muons which come from a decay of ordinary mesons generated in the first interaction, CORSIKA is run and the particle file is scanned for those muons which come

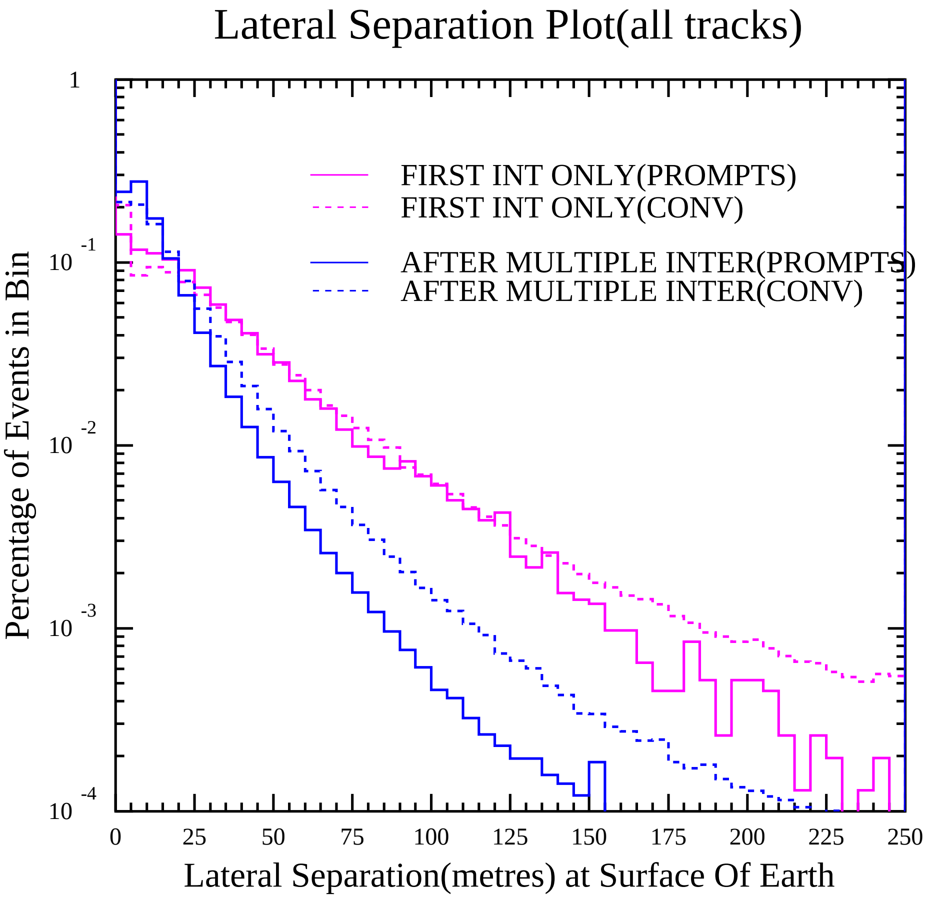

Figure 3.4: The distribution of lateral separation from shower core for the DPMJET-II for charm and coventional muons in each event with the first interaction and multiple interactions isolated.

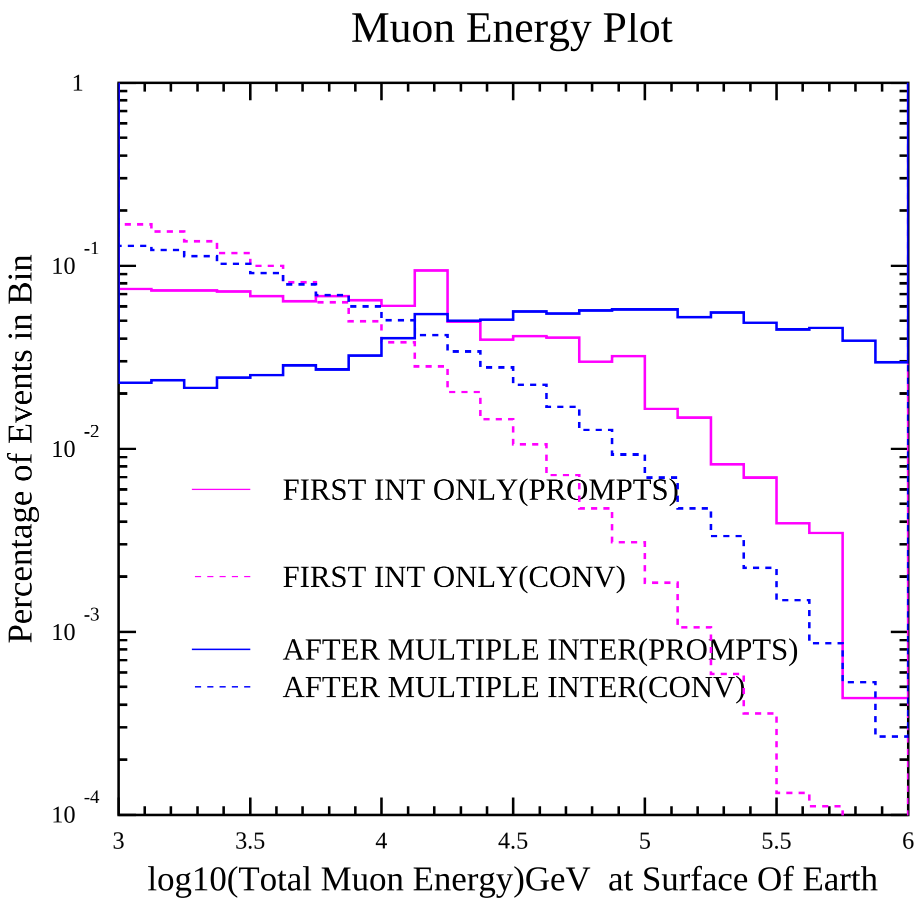

Figure 3.5: The total energy distribution for the DPMJET-II for charm and conventional muons for each event with first interaction and multiple interactions isolated.

from the first interaction by looking for the generation counter. In CORSIKA the generation counter is available that tracks the parents of the particles produced. For instance, for the decays from pions the counter is augmented by 51, for charmed particles it is 31 to get a discrimination against all other muons. The tagging could also be used to identify the muons from first interaction using the number on the generation counter during the production. If an event contains one or more muons that have their parent as a charmed particle we identify them as prompt muons. A need to tag the Prompt muon events was accomplished this way.

Chapter 4

Data streams and quality cuts on the 2005 Sample

4.1 First guess reconstructions, livetime and triggers

Likelihood reconstructions need a first guess for the muon track direction to be able to iterate through and get the final direction. The criteria for designing a first guess algorithm should be to have fast computing time while approximating the track direction. Two popular first guess algorithms are described below.

4.1.1 Direct Walk Reconstruction

Direct Walk is a pattern recognition algorithm. The basic algorithm reconstructs the track direction using only direct hits(hits unscattered in ice).

4.1.2 JAMS Reconstruction

JAMS (Just Another Muon Search) is a pattern recognition algorithm. The basic algorithm for JAMS creates hit selections and stores an event. A fast algorithm to find first guess candidate tracks is implemented using hit clusters and these are stored.

The first guess candidates are narrowed down into a few viable track solutions. One or two of these best track fits are stored in the event. The quality of the fit is measured by variable σ_ψ and in this analysis is set to be less than 0.05. It measures the deviation of hit clusters from a single track hypothesis.

During the 2005 data run, 1.85 billion events were recorded by AMANDA-II. The livetime for the 2005 filtered data is 199.25 days. The 2005 data filtering is different from earlier years in two aspects [19].

1. Modified cross talk is applied.
2. JAMS and Direct Walk at level 1 and level 2 cuts are swapped

The discussion in this chapter is confined to the analysis of downgoing muons. The output streams relevant to our analysis are the high quality stream and the minimum bias stream.

4.1.3 High quality stream

Downgoing muon events near the horizon with a high quality in JAMS reconstruction were selected. Every event with a zenith angle greater then 55 degrees in JAMS reconstruction fit with a low number for the spread $\sigma_\psi < 0.05$ of its JAMS fit solutions was identified in this stream.

4.1.4 Minimum bias stream

Every 100th event regardless of how it was triggered was included in this stream.

4.2 Reconstruction Methods

An arrival timing based likelihood approach as described by the Pandel function [13] was used to reconstruct the 2005 experimental data and simulation. This function was subsequently modified for PMT jitter and and a convoluted pandel probability distribution function was used for this analysis.

4.3 Techniques to Further Improve Background Rejection

Several other techniques were used to improve background rejection. Methods were also employed to remove electronic crosstalk and other fake events. The quality of the JAMS fit was checked to ensure high quality events

4.4 Event Simulation and Reweighting

This analysis relied on simulated data sets of background and signal events. The downgoing conventional atmospheric muons were simulated using the DPMJET-II.55 and SYBILL interaction models. For this work, a preliminary version of CORSIKA in which the charmed particle decays are enabled in DPMJET-II.55 [20] was used for signal simulation. Further, we know that the threshold primary energy for muons at large zenith angles to make it to the detector is high so we do the simulation in two stages to get enhanced statistics at large zenith angles.

1. Primary threshold energy of 800 GeV of primary cosmic ray energy for muons between 0 to 70 degrees zenith angle.

2. Primary threshold energy of 10 TeV for primary cosmic ray between 70 to 90 degrees zenith angle.

The events were simulated with a $\Phi \propto \mathrm{E}^{-1.7}$ primary energy spectrum, one power harder than the spectrum present in nature. The advantage of this approach is that it reduces the simulation time. The generated events must then be reweighted to the original cosmic ray spectrum with appropriate normalization factor applied [17].

4.4.1 Preparation of Simulated Events

It would be a huge demand on computer time to simulate the same number of days livetime worth of simulation as actual experimental data. Simulation is thus generated with a flatter spectra and event weights are used to reweight to the spectra we wish to simulate [18]. The simulation events were scaled to match the livetime of the data during a particular period or year. The simulated events underwent the same reconstruction procedures as the data and had to satisfy the same zenith angle and energy requirements. The reconstructed muons deviate from their actual direction due to mis-reconstruction and we use quality criteria to improve the angular resolution.

Chapter 5

Response of AMANDA-II to Cosmic Ray Muons

The flux of downgoing muons detected by the AMANDA-II neutrino telescope is used as a test beam to check the experimental systematic error and to improve the knowledge of its response. This work shows the outcome of the effort for a better understanding of AMANDA-II performance, an improved data filter and event reconstruction. The simulated predictions for preliminary experimental downgoing muon angular and depth intensities are compared with experimental results and theoretical calculations. This report encompasses large statistics of simulated data generated at large zenith angles using the QGSJET interaction model with a live time of 30 days and compared to a 30 day span of experimental data for the year 2001. This was aimed to minimize the effect of statistical and systematic errors on the angular and depth intensities (particularly close to the horizon). The use of a new Convoluted Pandel likelihood function ensures improved event reconstruction and stability. This also ensures good agreement between simulated and experimental data. Further, analysis was also done using the 2005 experimental data and 2005 simulation using the

SYBILL interaction model. CORSIKA air shower generator was used to simulate the interaction of the cosmic rays with the atmosphere.

5.1 Analysis

In order to measure the atmospheric muon angular distribution it is necessary to evaluate the event trigger and reconstruction efficiencies as a function of the zenith angle. This requires a Monte Carlo with the complete simulation chain from the primary interaction in the atmosphere to the detector response based on best knowledge of the physical processes involved. The event generation is done using CORSIKA v6.020 with the QGSJET01 interaction model. The model incorporates the curvature of the earth and the south pole average atmospheric profile. A multi-component primary cosmic ray energy spectrum [5] is used to get the composition. The generated muons are propagated to the earth's surface and then through the ice, considering all pertinent energy losses. The muons passing through AMANDA-II or near it are folded into the detector trigger simulation. At this stage the detector response is completely simulated in order to reproduce the experimentally detected events. This is based on our overall understanding of the physics and the detector.

The event reconstruction chain for simulation is identical to the one used for the experimental data. A cleaning procedure then removes the optical modules that are dead or have odd transient behavior. A time calibration which also accounts for the signal propagation time through the cables is then employed. A Convoluted Pandel probability distribution function (a time likelihood based reconstruction) is used. This accounts for the finite photo-multiplier tube timing resolution of the pulse obtained when a photon emitted by the muon passes through it. Due to the limited angular resolution of the reconstruction, additional cuts are used to improve the event sample quality for both the experimental and simulated data. These cuts improve the resolution of the zenith angle and the space angle. .

Tables 5.1 and 5.2 summarize the mean, median, RMS and the extreme tail of the zenith angle and the space angle resolution. We misreconstruct events closer to the horizon and this becomes more prominent as we get closer to the horizon. This can partially be explained by the fact that vertical muons would have larger track length and larger number of direct hits (hits that are minimally scattered in the ice before being detected by a optical module) and hence their direction determined more accurately than a horizontal event. With this resolution we can derive the experimental angular distribution at AMANDA-II depth by merely calculating the detector acceptance at each zenith angle bin using the simulated detector response to unfold the measured data, neglecting the inter-bin correlations. When we neglect interbin correlations, for each bin in cosine of the zenith angle, the ratio of the true events generated (that trigger AMANDA) to the reconstructed events (accounting for various efficiencies during reconstruction) for both the Monte Carlo simulation (known ratio) and the corresponding experimental data (unknown ratio) can be equated. With interbin correlations, one needs to account for leakages across bins due to finite angular resolution and event quality. Neglecting inter-bin correlations can be justified by demonstrating that these correlations are minimal. We accomplish this by making our best event quality selections on a sample of 30 days of simulation data. The quality cuts chosen for this purpose are chi square for the reconstructed track less than 7.3, track length greater than 120 meters(-15ns to 75ns direct hits only), absolute value of the the difference between the zenith angle reconstructed using odd hits only and using even hits only from hits ordered. Further these inter-bin overlaps can be minimized by increasing or decreasing the bin size in cosine zenith. The bin-size for the actual intensity distribution is defined at twice the RMS value of statistics shown in tables 5.1 and 5.2 so that most events are self contained and overlaps are minimal. This implies we need to use larger bin sizes to account for poorer angular resolution closer to the horizon. Experimental data spanning 30 days from the year 2001 is used.

5.2 Results

Ice properties(scattering and interaction lengths) are an important uncertainty that affects the count rates of muons in the Monte carlo simulation when results are shown. In this chapter in particular and the thesis in general we use three models. MAM (Muon Absorption Model) is obtained by increasing the absorption such that the time residuals match between the data and the Monte Carlo. It includes the effect of OM sensitivity as well as ice model and is based on the model of layered ice. The millennium ice model incorporates actual AMANDA ice measurements and is believed to be more accurate than the MAM model. A new and a better ice model called the AHA incorporates "stretched" layer structure, i.e., dust peaks are higher and valleys lower and corrects for the systematic smearing of the layers with the measurement techniques used in AMANDA [10].

Figure 5.1 shows the plot of the angular distribution of downgoing muons in the AMANDA-II detector (the flux of atmospheric muons versus the cosine of the zenith angle) using the 2001 experimental data. The triangles represent the AMANDA-II detector data and the boxes represent the simulated data. The plot shows simulated data using the MAM ice model. Figure 5.2 shows the atmospheric muon flux as a function of slant depth. The slant depth is a function of the zenith angle and represents the distance the muon travels to the AMANDA depth. Imagine looking at the surface of the Earth from the AMANDA depth at different angles. Figure 5.3 and figure 5.4 shows the comparison between the simulation and experimental data. It can be seen that the experimental data and the simulation differ by about 25% for vertical muons and is as high as 40-45% for horizontal muons.

Likewise, figures 5.5, 5.6, 5.7, 5.8 represent similar plots for the 2005 experimental data and SYBILL millenium model. Better angular resolution was also ensured using tighter quality cuts compared to the earlier MAM ice model. Figure 5.7 and 5.8 show the comparison between the simulation and experimental data and is a measure of performance of our simulations to replicate experimental data and helps us understand the systematic error. It can be seen that the experimental data and the simulation differ by only 10-20% till 80 degrees in zenith angle when the Millenium SYBILL Monte Carlo is used.

Figure 5.11 shows the comparison of the down going muon intensity as measured by the L3+C collaboration. It can be noticed that hadronic interaction model QGSJET01 has the maximum disagreement with the observed data while SYBILL has the minimum difference.

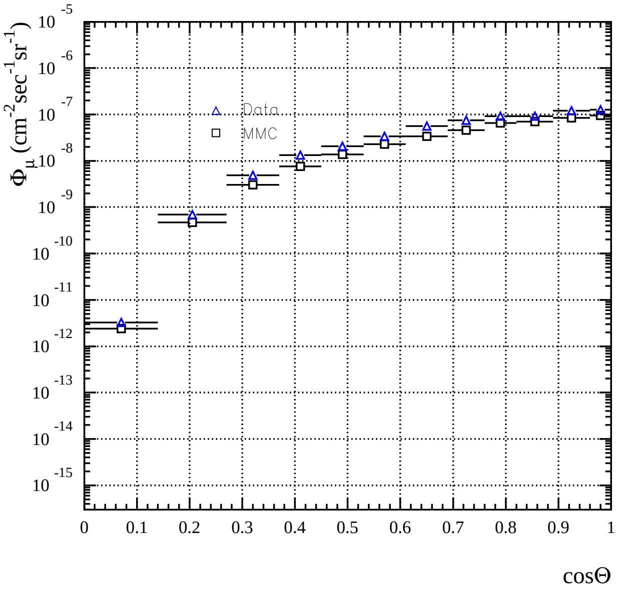

Figure 5.1: The angular distribution of atmospheric muons in AMANDA-II at a depth of 1730m using the MAM ice model with the SYBILL interaction model and the 2001 experimental data.

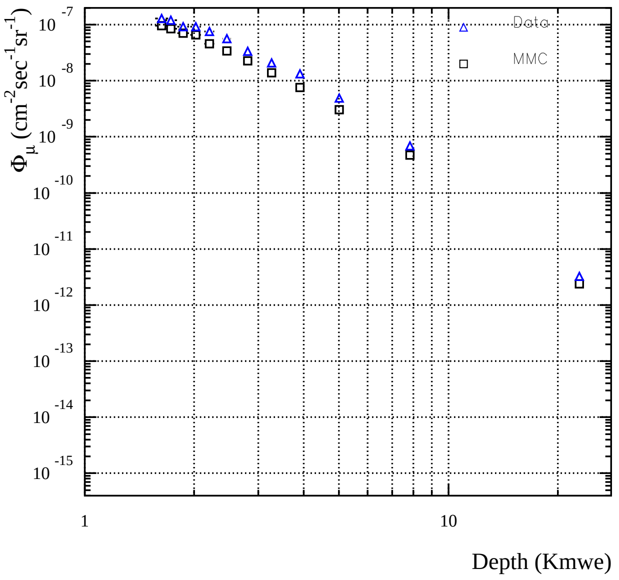

Figure 5.2: The depth-intensity of atmospheric muons in AMANDA-II using the MAM ice model and the SYBILL interaction model with the 2001 experimental data.

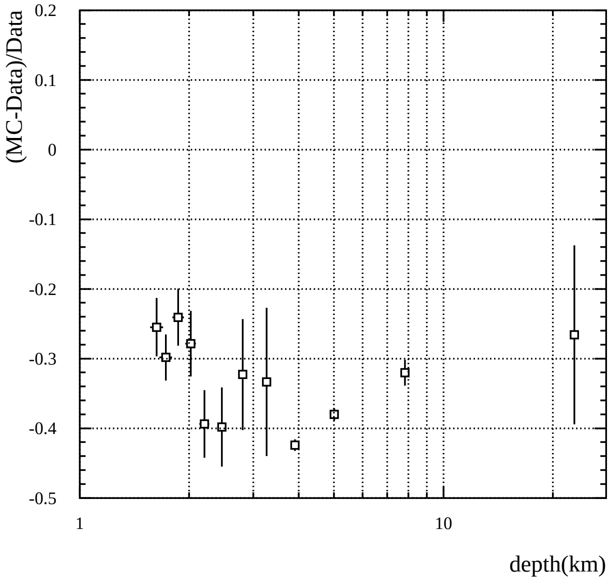

Figure 5.3: The relative difference between MAM SYBILL Monte Carlo and AMANDA-II 2001 data as a function of depth.

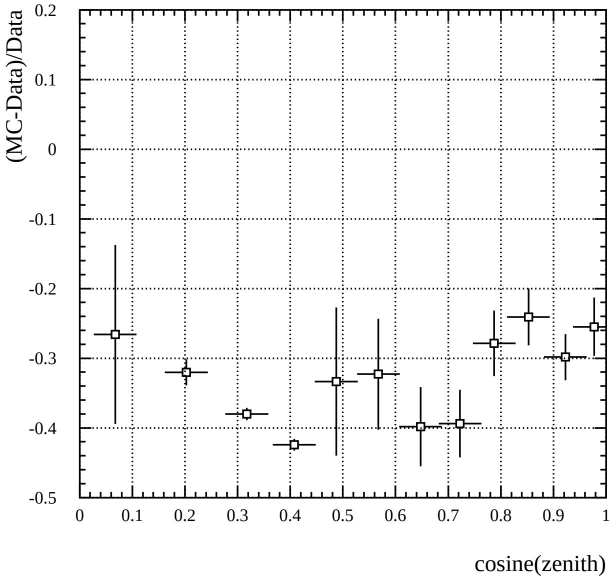

Figure 5.4: The relative difference between MAM SYBILL Monte Carlo and AMANDA-II experimental data as a function of zenith angle.

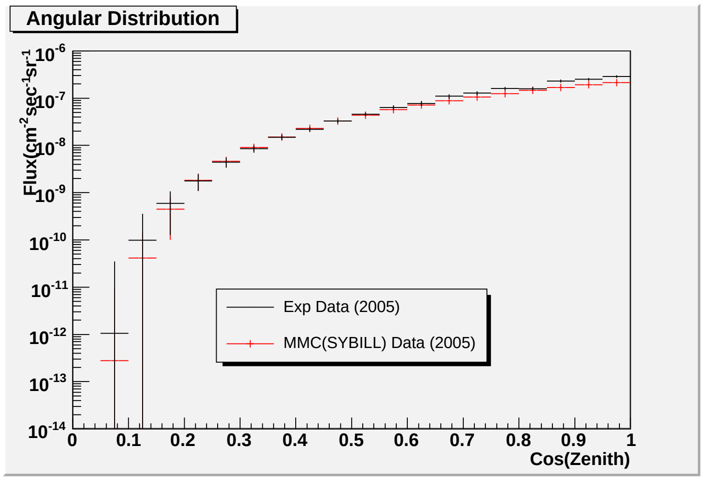

Figure 5.5: The angular distribution of atmospheric muons in AMANDA-II at a depth of 1730m using the Millenium ice model with the SYBILL interaction model and the 2005 experimental data.

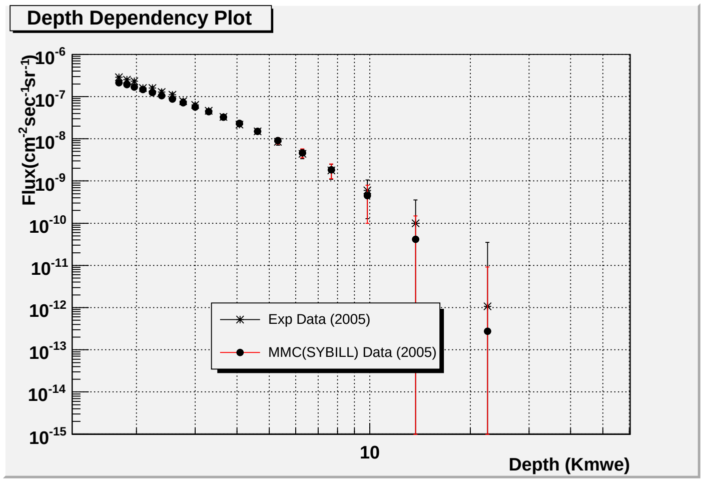

Figure 5.6: The depth-intensity of atmospheric muons in AMANDA-II using the Millenium ice model and the SYBILL interaction model with the 2005 experimental data.

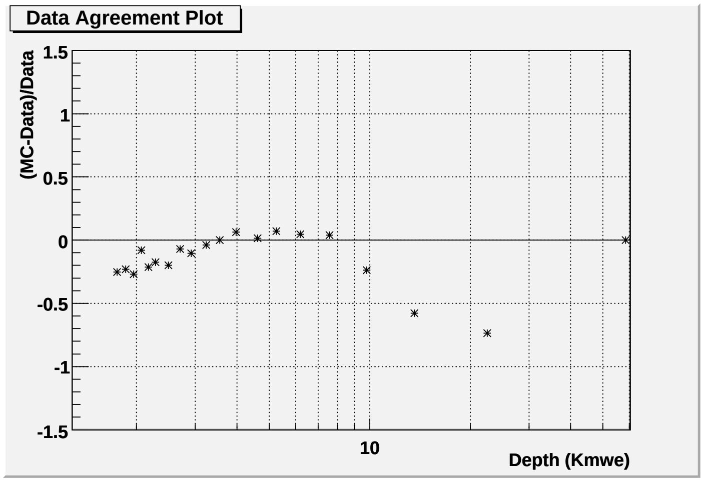

Figure 5.7: The relative difference between Millenium SYBILL Monte Carlo and AMANDA-II 2005 experimental data as a function of depth.

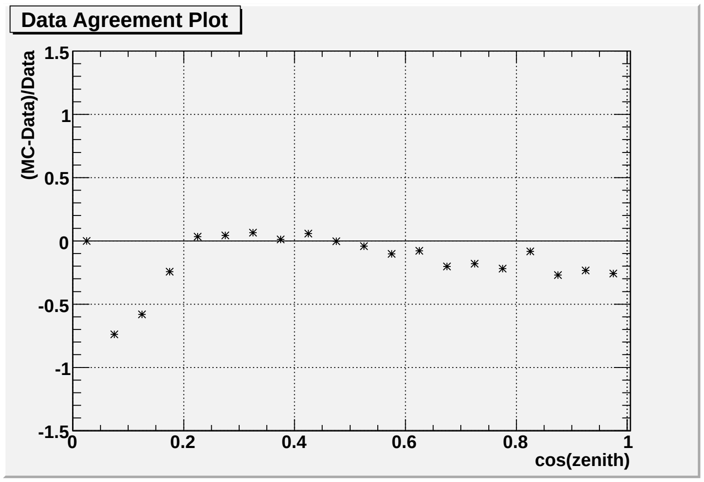

Figure 5.8: The relative difference between Millenium SYBILL Monte Carlo and AMANDA-II 2005 experimental data as a function of zenith angle.

cos (zenith)	**Mean (degrees)**	**Median (degrees)**	**RMS (degrees)**	**90% quantile right(degrees)**	**90% quantile left(degrees)**
0.0-0.05	14.23(21.22)	11.75(22)	7.11(5.55)	25.5(28.0)	7.0(+13.0)
0.05-0.1	8.02(19.10)	6.75(19)	5.09(6.55)	16(27.0)	3.0(+10.0)
0.1-0.15	5.27(15.49)	4.5(15.5)	4.14(7.01)	11.75(25.0)	1.0(+6.0)
0.15-0.20	3.22(11.46)	2.75(11)	3.34(6.96)	7.5(21.0)	-0.2(+2.5)
0.20-0.25	2.36(8.04)	2.0(7.0)	2.93(6.34)	6.0(18.0)	-0.75(+0.5)
0.25-0.30	1.77(5.6)	1.6(4.5)	2.71(5.51)	5.0(14.0)	-1.25(-0.5)
0.30-0.35	1.43(3.86)	1.2(3.0)	2.57(4.76)	4.0(11.0)	-1.75(-1.5)
0.35-0.40	1.17(2.6)	1.0(2.0)	2.45(4.13)	4.25(8.5)	-1.75(-2)
0.40-0.45	0.97(1.55)	0.7(1.5)	2.34(3.64)	4.0(6.5)	-1.9(-2.75)
0.45-0.50	0.69(1.55)	0.6(0.75)	2.13(3.26)	3.5(4.5)	-2.0(-5.5)
0.50-0.55	0.84(1.99)	0.25(1.25)	2.26(4.96)	4(8)	-2(-3)
0.55-0.60	0.53(1.63)	0.5(1)	2.24(4.88)	3.5(7.5)	-2(-3)
0.60-0.65	0.53(1.41)	0.5(0.5)	2.25(4.86)	3.75(7)	-2(-3.5)
0.65-0.70	0.51(0.99)	0.12(0.75)	2.06(4.57)	3.0(6)	-2(-3.5)
0.70-0.75	0.30(0.74)	0.12(0.5)	1.98(4.39)	2.5(5.5)	-2(-3.5)
0.75-0.80	0.29(0.49)	0.12(0.5)	1.79(4.30)	2.5(5)	-2(-3.5)
0.80-0.85	0.21(0.30)	0.12(0.25)	1.75(4.21)	2.0(4.5)	-2(-3.5)
0.85-0.90	0.17(0.05)	0.1(0.25)	1.72(4.09)	2.0(4.5)	-2(-4)
0.90-0.95	0.13(-0.30)	0.1(0.0)	1.77(3.98)	2.25(3.8)	-2(-4.5)
0.95-0.1.0	-0.14(-1.05)	0.1(-0.5)	1.94(4.12)	2.0(2.75)	-2.5(-5.75)

Table 5.1: Presents the statistics of zenith angle resolution after quality cuts for various zenith ranges. Values in brackets are before quality cuts for the QGSJET model.

cos (zenith)	**Mean (degrees)**	**Median (degrees)**	**RMS (degrees)**	**90% quantile (degrees)**
0.0-0.05	16.25(24.34)	9.13(24.5)	2.72(7.30)	26(34)
0.05-0.1	9.88(21.21)	6.63(21)	2.29(7.91)	19(32)
0.1-0.15	6.85(17.6)	4.39(17)	2.73(8.4)	13(29)
0.15-0.20	5.34(13.95)	3.79(12.75)	8.3	10(25.2)
0.20-0.25	4.63(10.95)	3.23(9.2)	7.7	8.9(21.2)
0.25-0.30	4.31(9.05)	3.0(7.2)	6.9	8.0(18.2)
0.30-0.35	4.10(7.75	2.9(6.05)	6.14	7.9(16)
0.35-0.40	4.00(6.88)	2.76(5.5)	5.55	7.8(13.2)
0.40-0.45	3.84(6.22)	2.62(5.0)	5.11	7.0(12.0)
0.45-0.50	3.63(5.65)	2.47(4.5)	4.81	6.8(11.0)
0.50-0.55	3.87(6.63)	2.72(5.0)	6.04	7.0(13.5)
0.55-0.60	3.16(6.3)	2.29(4.75)	5.68	6.0(13.5)
0.60-0.65	3.47(6.17)	2.7(4.5)	5.62	6.3(13.0)
0.65-0.70	3.20(5.91)	2.17(4.5)	5.33	6.0(12.5)
0.70-0.75	2.98(5.58)	2.04(4.2)	5.16	5.75(12.0)
0.75-0.80	2.73(5.31)	1.84(4.0)	4.99	5.1(11.5)
0.80-0.85	2.65(5.13)	1.92(3.75)	5.01	5.0(11.0)
0.85-0.90	2.56(5.09)	1.88(3.75)	5.00	5.0(11.0)
0.90-0.95	2.61(5.13)	2.0(3.75)	5.2	5.0(11.0)
0.95-0.1.0	2.89(5.14)	2.3(3.75)	5.18	5.7(11.0)

Table 5.2: Presents the statistics of space angle resolution after quality cuts for various zenith angle ranges. Values in brackets are before quality cuts for the QGSJET model.

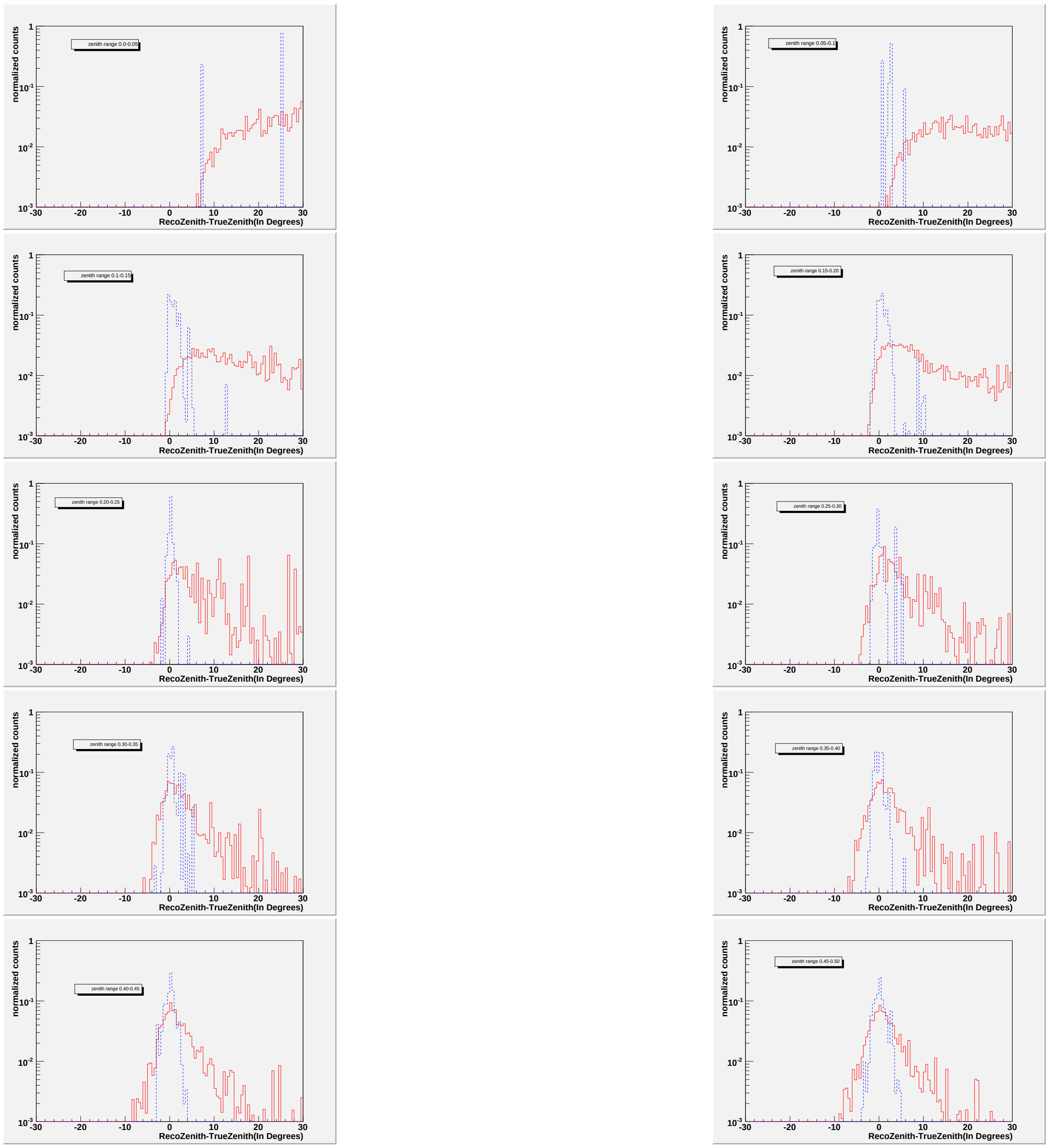

Figure 5.9: The zenith angle difference between the reconstructed and true zenith angle known from simulation is plotted on x-axis while normalized counts are plotted on y-axis. The respective slices in zenith are indicated in the plot. Red is before quality cuts while blue is after quality cuts. From left to right and top to bottom there are 10 slices shown that go from 0.0-0.5 in increments of 0.05.

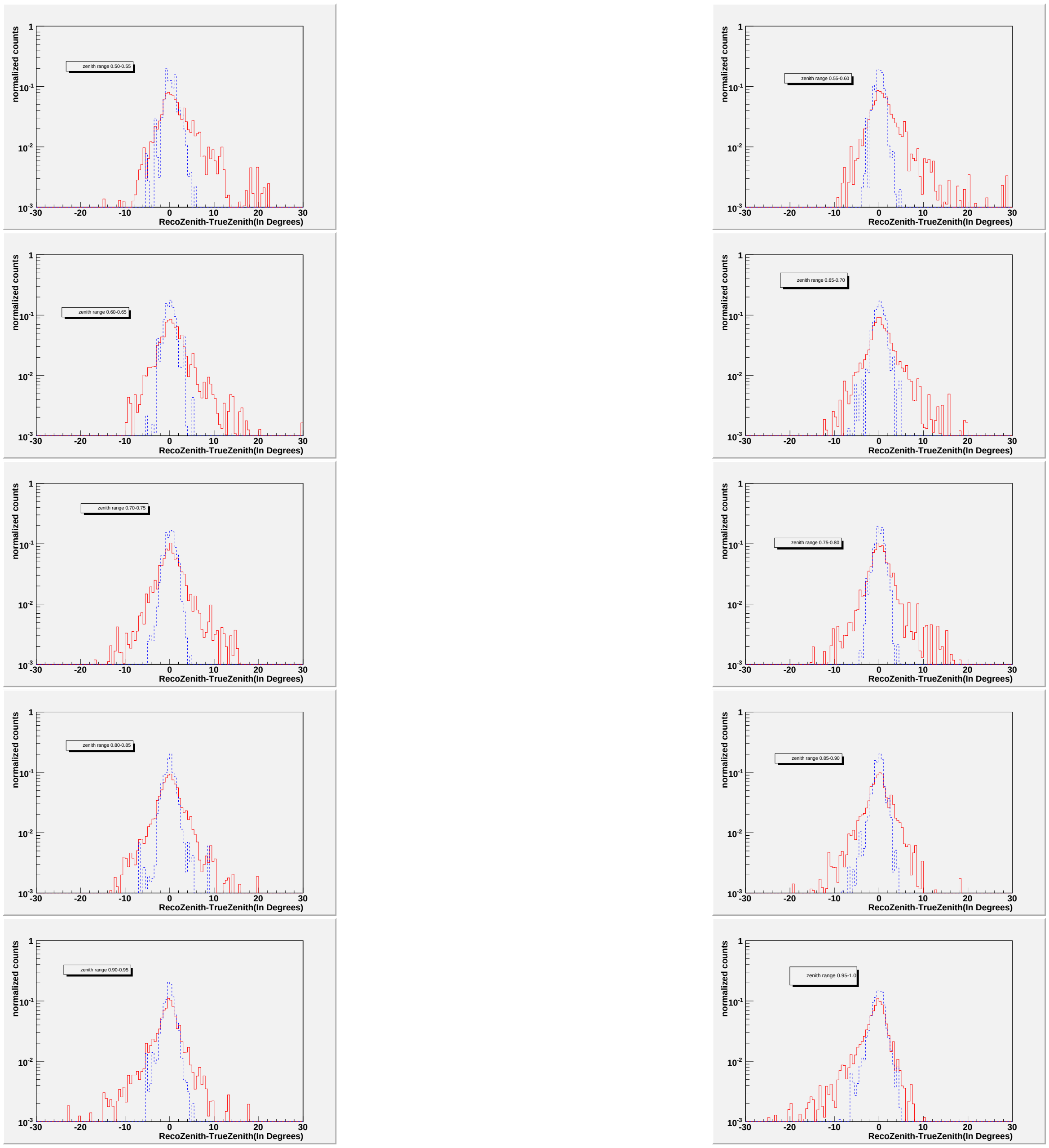

Figure 5.10: The zenith angle difference between the reconstructed and true zenith angle known from simulation is plotted on x-axis while normalized counts are plotted on y-axis. The respective slices in zenith are indicated in the plot. Red is before quality cuts while blue is after quality cuts. From left to right and top to bottom there are 10 slices shown that go from 0.5-1.0 in increments of 0.05.

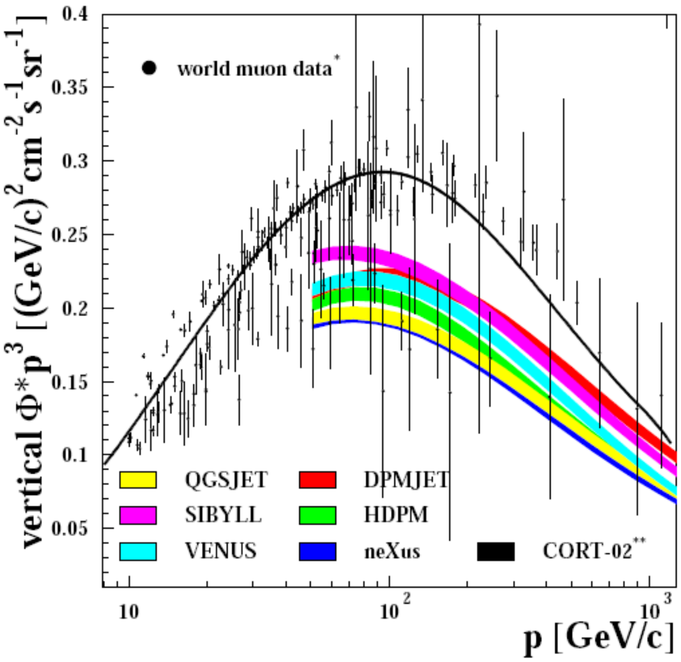

Figure 5.11: Comparison of CORSIKA vertical muon flux for various interaction models.

Chapter 6

Model dependencies and systematic error calculations for a down-going muon analysis

Traditional cut and count analysis place a limit or make a discovery based on excess of events over the predicted background in the experimental data. Due to uncertainties in the simulation, the number of signal and background events predicted may not accurately reflect the true signal and background numbers. The cosmic ray spectrum is uncertain both in normalization and spectral index. There are also detector-related uncertainties due to the uncertain sensitivity of optical modules and modeling of light propagation. Different interaction models produce different number of muons and there is a wide variety of choices of models but by far the biggest uncertainty affecting this analysis is the ice. Our incomplete understanding of the dust layers in the ice makes ice a nuisance parameter that affects the sensitivity to the prompt muon signal. For purposes of computing final results we use two models, the AHA and the Millenium ice models without being biased to either but allow the fit to decide the right proportions of these models to explain the experimental data. The systematic uncertainties are summed in quadrature separately for background and signal. These uncertainities are a useful exercise to determine the mismatch between experimental data and simulation that could be used for any future downgoing muon analysis.

Due to the nature of uncertainties and difficulties in quantifying them we deviate and take another approach that is based on shape based fitting for background and signal to experimental data for calculating the final limit.

6.1 Statistical Errors

Due to the computational requirements, background and signal simulation statistics are somewhat limited. However, the optimized background simulations used in this analysis have large variation in event weights (we use a reweighted MC simulation). The statistical errors are kept track by ROOT and these were subsequently used for the construction of the limit.

6.2 Systematic Uncertainties

6.2.1 Normalization of Cosmic Ray Flux

The different absolute normalizations between the experiments are caused by uncertainities in the energy calibration. The average energy of cosmic ray particles is $4.4*10^7$ GeV, which is considerably above the knee in the all-particle cosmic ray spectrum. Numerous experiments have measured a large spread in the absolute normalization of the flux of cosmic rays at this energy [9]. Estimates of the uncertainty in the normalization of the Horandel cosmic ray flux are 20% [5]. This uncertainty translates to a 20% variation in the number of background and signal events.

6.2.2 Spectral Index of Cosmic Ray Spectrum

The best fit values for the spectral index of the cosmic ray data is -2.71±0.02 in which the errors specify the statistical uncertainties [5]. Varying the spectral index by 0.02 in the DPMJET-II interaction model (model being tested) produces an average variation of 35% in the number of background and signal events in the High-Energy region ($N_{\mathrm{ch}} \geq 400$) as is shown in figure 6.1. The corresponding plot with the actual number of event counts in one year of data is shown in figure 6.2.

6.2.3 Detector Sensitivity

The properties of the refrozen ice around each OM, the absolute sensitivity of individual OMs, the obscuration of OMs by nearby power cables can effect the detector sensitivity. The analysis uses the values obtained in [6] where reasonable variations of these parameters in the simulation were found to cause a 15% variation in the signal and background passing rate.

6.2.4 Interaction Model Uncertainity

For this analysis, two interaction models SYBILL and DPMJET-II are considered equally likely options for the background simulation. Each of the these models were renormalized to match the number of data events observed in the low N_{ch} region, where the signal was expected to be insignificant compared to the background. By rescaling the simulation to the number of observed data events, the uncertainty of the background simulation was reduced to the uncertainty in the spectral shape. We have only one model of signal simulation (DPMJET-II) hence no uncertainty was assumed on it. Varying the models produces an average variation of 80% on the background in the high energy region ($N_{\mathrm{ch}} \geq 400$) as is shown in figure 6.3. The corresponding plot with the actual number of event counts in one year of data is shown in figure 6.4.

6.2.5 Ice Model Uncertainty

Based on results from ice properties systematics studies, the millennium ice model has been modified and a new ice model (called the aha model) has been constructed. Two types of modifications were made to the millennium model: a) the ice model was corrected for a systematic smearing of the dust layer structure introduced by the analysis methods used in AMANDA, and b) the extrapolation of the optical properties to larger depths was redone with new ice core data on dust concentration to produce cleaner ice below the big "dust peak". The details are explained in [10]. Varying the models produces an average variation of 40% on the background in the high energy region ($N_{\mathrm{ch}} \geq 400$) as is shown in figure 6.5. The corresponding plot with the actual number of event counts in one year of data is shown in figure 6.6.

6.2.6 Other Source of Errors

The systematic errors due to the rock density (below the detector), and muon energy loss do not contribute significantly to this analysis.

6.3 Result of Systematics Study

The systematic uncertainties are summed in quadrature separately for background and signal and the total systematic error numbers for background and signal are calculated to be 70% and 60% respectively.

Source Name	**Background simulation**	**Signal simulation**
Cosmic Ray Normalization	20	20
Cosmic Ray Spectral Index	35.0	35.0
Detector Sensitivity	15.0	15.0
Ice Properties	40.0	40.0
Interaction Model Uncertainty	40.0	X
Total Error	70.0	60.0

Table 6.1: Average simulation uncertainties for different sources of errors.

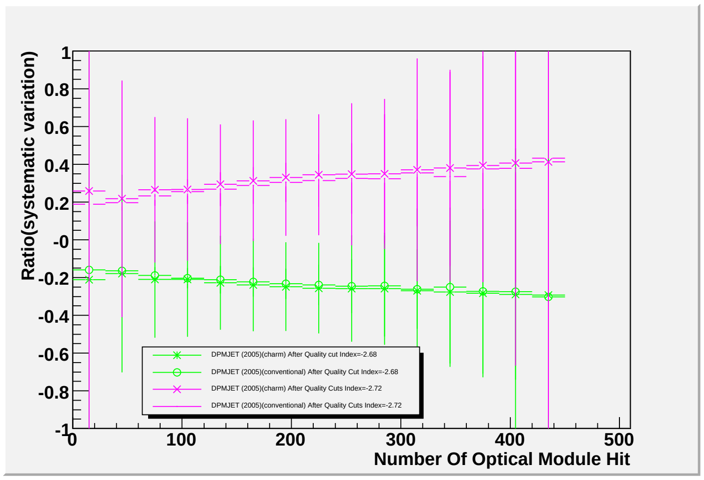

Figure 6.1: The N_{ch} variation for the DPMJET-II for signal and background (at the final level after event selection criteria are implemented) when spectral index is varied by ±0.02 shown as a ratio.

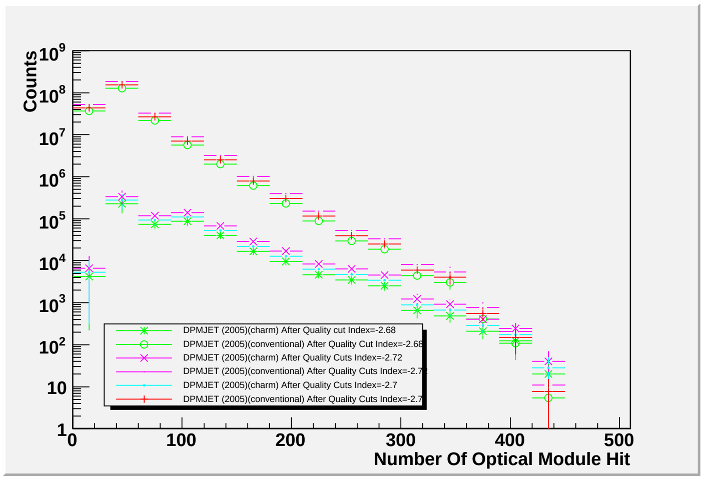

Figure 6.2: The N_{ch} distribution for the DPMJET-II for signal and background (at the final level after event selection criteria are implemented) when spectral index is varied by ±0.02 shown as a ratio.

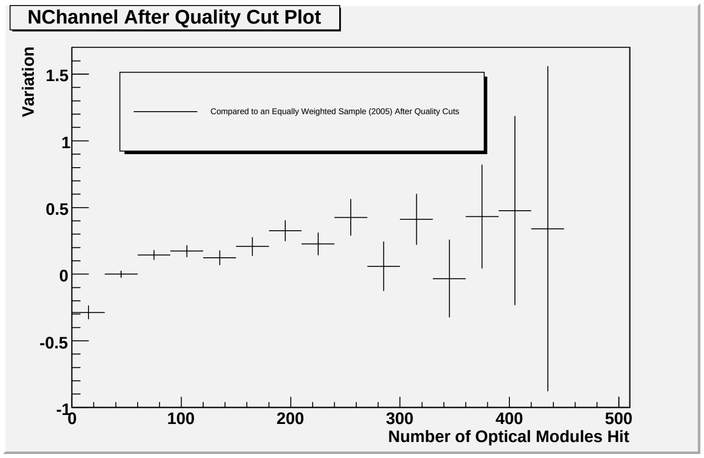

Figure 6.3: The N_{ch} variation for the DPMJET-II for background (at the final level after event selection criteria are implemented) when compared with an equally weighted simulation of SYBILL and DPMJET-II is shown.

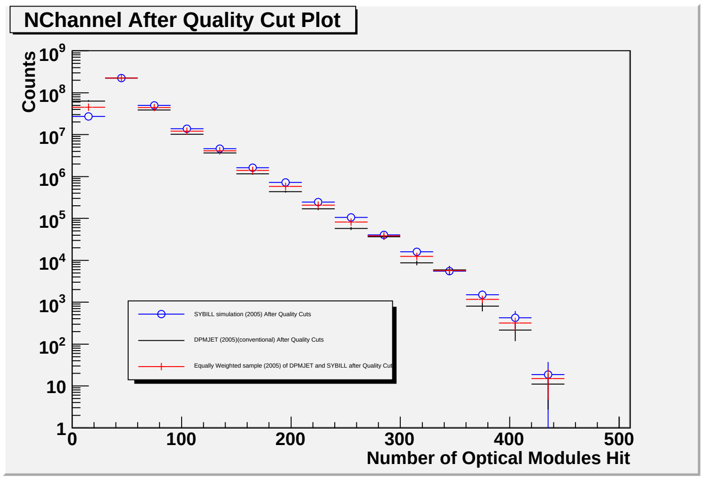

Figure 6.4: The N_{ch} distribution for the DPMJET-II for background (at the final level after event selection criteria are implemented) when compared with an equally weighted simulation of SYBILL and DPMJET-II is shown.

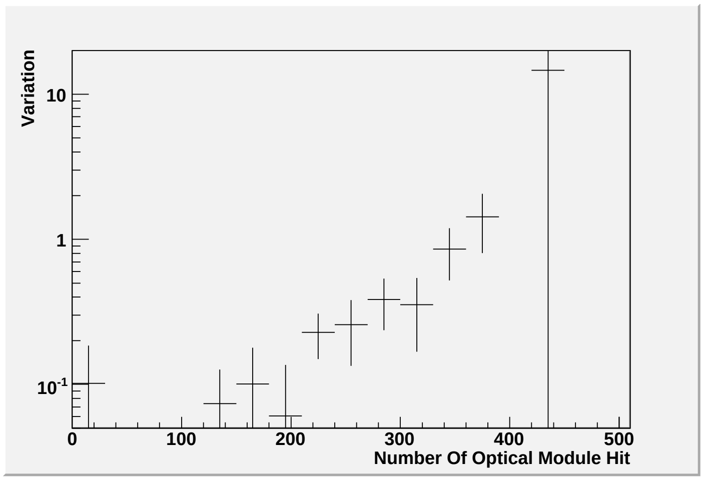

Figure 6.5: The N_{ch} variation for the DPMJET-II millenium ice model (at the final level after event selection criteria are implemented) when compared with an equally weighted simulation of DPMJET-II millenium and DPMJET-II AHA model is shown.

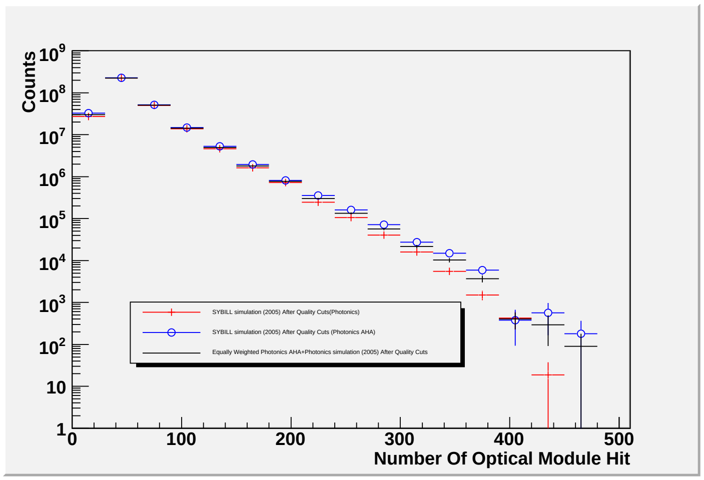

Figure 6.6: The N_{ch} distribution for the DPMJET-II millenium ice model (at the final level after event selection criteria are implemented) when compared with an equally weighted simulation of DPMJET-II millenium and DPMJET-II AHA model is shown.

Chapter 7

Hadronic Interaction Models and Extended Air showers

7.1 Introduction

The development of a shower is influenced by the properties of the hadronic interactions and the mechanisms of the transport of secondary particles through the atmosphere in addition to the primary cosmic ray mass and energy. The hadronic and nuclear interactions impose large uncertainties since they are poorly known in the energy and kinematic ranges of interest. In addition, a detector with its limited acceptance and efficiency gives a distorted picture of the secondary particles. The challenge of experimental physics is to understand the shower development and the detector performance well enough using the experimental data obtained and to gain an understanding of hadronic and nuclear interaction models.

In the shower development process major uncertainities arise from the hadronic interactions which are described by phenomenological models. These models are tuned to fit the available data from $p - \bar{p}$ and heavy ion accelerators but the experimental data are not well suited for CR interactions. Collider experiments do not register the most energetic particles emitted in the extreme forward direction which are key to atmospheric shower development and accelerators by far do not reach the energies encountered in cosmic rays. This extrapolation to higher energies relies solely on theoretical guidelines and the uncertainities play a huge role.

The muon rate as measured by the AMANDA-II detector is higher by about 30% than simulations using the QGSJET model with the Wiebel-Sooth parametrization for the cosmic ray spectrum [25]. Comparisons like these indicate that more benchmarks with data and improvements of the hadronic interaction model are necessary. A comparison of interaction models in CORSIKA [26] when used in its interaction test mode for beams of monoenergetic protons on nitrogen nuclei (the most abundant component of air) is presented. In this mode only the first interaction of a shower calculation is performed.

All secondaries from CORSIKA including the spectator nucleons from projectile and target, are stored in the particle stack, and further shower calculations are omitted. In this mode, many interactions can be generated, and all information about the particles can be stored. In the released CORSIKA version, charmed hadrons cannot be handled properly. In this work we have a preliminary version of CORSIKA in which the charmed particle decays are enabled in the framework of DPMJET-II.55 [20] hadronic interaction model. The energy fractions, multiplicities and Z-moments of these particles are compared to the FLUKA+DPMJET-III [27] hadronic interaction and transport code. For model comparison we have used both diffractive and non-diffractive events in a mixture as given by respective models. Diffractive events are visible as peaks at large energy fractions, as events typically have a forward-going meson with a direction slightly different from that of the original proton.

It is suggested in [30] that prompt muons become dominant at large distances from shower core due to their larger transverse momentum. DPMJET-II model (with charmed particles allowed to decay) is used to test this hypothesis and lateral muon density distributions characterizing the region of high energy and large zenith angle are shown and these distributions are isolated for the first interaction (showering off) and multiple interaction (showering on) for the following cases:

a) Cosmic ray spectrum

b) Cosmic ray spectrum with zenith angle greater than 80 degrees

c) Showers with 1-1000PeV primary energy

d) Monoenergetic primary energy of 1PeV.

Events involving prompt muon (atleast one or more prompt muons) and conventional muon (no prompt muon) are distinguished. Characterization of the hardness of the energy and zenith angle spectra of prompt muons compared to conventional muons are shown in the framework of DPMJET-II.55 hadronic interaction model.

7.2 Interaction and Extended Air Shower models

7.2.1 Available Codes and Model Comparisons

CORSIKA [26] is a multi-purpose shower simulation program of air shower development. The hadronic interaction models DPMJET, QGSJET-I [28] and QGSJET-II [29], SYBILL in CORSIKA are studied and compared with the predictions from the FLUKA model. QGSJET and DPMJET are based on the Gribov-Regee theory of multi-Pomeron exchange, which has been used successfully for over a decade to describe elastic and inelastic scattering of hadrons. In particular nucleus-nucleus collision and diffraction are treated in great detail in these models. SIBYLL [22] is a minijet model that describes the rise of the cross-section with energy by increasing the pairwise minijet production and also applies the Glauber theory for hadron-nucleus collisions and treats projectile nuclei as a superposition of free nucleons. PYTHIA [32] models hadronic interactions with high momentum transfer according to QCD, and takes into account resonance formation as well as gluon radiation from quarks and contains the fragmentation of colour strings into colour neutral hadrons. It also contains the soft processes which are important for air showers, but cannot handle primary mesons or nucleus-nucleus collisions on the basis of classical string theory. For treatment of nucleus-nucleus collisions FRITIOF adopts superposition principle. Hence a combination of PYTHIA and FRITIOF should be used to simulate EAS. The major systematic uncertainities in EAS analysis arise from the lack of knowledge of the total cross-sections and the details of particle production for nuclear and hadronic reactions at high energies with small momentum transfer.

7.2.2 Cross Sections

The first quantities compared are the inelastic p-air cross-sections. All models except for SYBILL calculate cross-sections from the experimental data assuming a distribution of the nucleons in the air nuclei. Therefore, all these models agree reasonably with each other (and collider data) and start to diverge only at energies where no measurements exists anymore. SYBILL adopts a parametrization which exhibits the flattest rise with values clearly below the experimental results at lower energies and steeply rises and surpasses all other models at higher energies. In DPMJET-II.55 this has been corrected downwards and agrees nicely with the cross sections Of QGSJET. The spread between the models amounts to about 35% as shown in figure 4.12. Since the inelastic cross-section determines the mean free path of a particle in the atmosphere, it influences directly the longitudinal shower development. A larger cross-section causes shorter showers and consequently, fewer particles at ground level. The differences in cross-sections for comparable assumptions originate partially from different applications of the Glauber theory and from varying assumptions regarding the form of the target nuclei. The discrepancies between the models are rather big, taking into consideration that all authors use basically the same approach to calculate cross-sections. By agreement on the best method of calculation a big part of the discrepancies should vanish.

7.2.3 Particle Production

The production of secondaries in hadronic interactions also differs between models. A variety of quantities need to be examined.The quantity with the largest impact on air shower development is the inelasticity ,i.e. the fraction of the energy of a particle that is used for production of secondary particles. Again, a variation in this quantity directly implies a modification of the longitudinal shower development. The effects of inelasticity and cross-sections are basically independent and may cancel out or add up. For DPMJET with the largest inelasticity and the largest cross-sections the showers are very short and this leads to differences in the muon multiplicity at the ground level and depth of detector.

7.2.4 Impact of shower simulations

In interpretation of shower measurements,it is vitally important to make a common effort towards a reference simulation program that contains the best and the most detailed treatment of all physical processes relevant to shower development that are used and tested by each experiment in a different way. Such a reference should also serve to estimate the performance of special purpose programs that are optimized for particular aspects of CR physics such as calculations of highest energy showers, TeV muons, Cherenkov light production, and so on. Air shower analyses are based on the comparison of experimental data with MC simulations and so to be able to perform such a comparison, a spectral form, an energy dependent mass composition and parameters of the high-energy interactions have to be assumed. Therefore, a discrepancy between MC and data can have many sources and on the other hand an agreement does not necessarily mean that all assumptions are right especially when registering only one observable (i.e. number of muons); several parameter settings may exist that can reproduce the observation. Fluctuations in the observable are then directly projected onto uncertainties in the primary energy or mass. When measuring several quantities it is possible to recognize fluctuations. A big part of the shower fluctuations originates from the first hadronic interaction and the secondary particles produced are studied. It has been noted earlier that the SYBILL model predicts fewer muons for high-energy air showers as compared to other models. Several hadronic observables have been investigated and compared to various hadronic interaction models. Correspondingly, they are characterized by a restricted number of adjustable parameters, which can be fitted with the available data. However the microscopic content of any model is restricted by only a number of possible physics mechanisms. Thus, one can not exclude the possibility that something important is missing, especially, concerning the very high energy range. This explains the need for alternative model approaches and for continuing tests of model validity, using both accelerator and cosmic ray data.

7.3 Results

7.3.1 Interaction Model

A comparison of interaction models in CORSIKA when used in its interaction test model for beams of monoenergetic protons on nitrogen nuclei is done. In this model only the first interaction of a shower calculation is performed and high-statistics proton beams in the energy range from 1TeV to 100PeV were used. All secondaries, including the spectator nucleons from projectile and target, are stored in the particle stack, and further shower calculations are omitted. In this mode, many interactions can be generated, and all information about the particles can be stored. In the released CORSIKA version, charmed hadrons cannot be handled properly. For this work we have used a preliminary version of CORSIKA in which the charmed particle decays are enabled in DPMJET-II.55 [20]. The energy fractions, multiplicities and Z-moments of these particles are compared to the FLUKA+DPMJET-III interaction and transport code. For model comparison we have used both diffractive and non-diffractive events in a mixture as given by respective models. Diffractive events are visible as peaks at large energy fractions, as events typically have a forward-going meson with a direction slightly different from that of the original proton. From figure 7.1 we see that SIBYLL and FLUKA + DPMJET-III are in very good agreement with each other and in reasonable agreement with DPMJET-II for conventional mesons (pions and kaons). However, QGSJET-01 [28] and QGSJET-II [29] predict a lower energy fraction in the diffractive region where secondaries take a very large fraction of the primary energy. This could explain the disagreement in the AMANDA-II muon intensity distribution , since the depth of the detector selects higher energy secondaries. The fact that AMANDA data are about 30% higher than simulations [25] indicates that models like SIBYLL, FLUKA+DPMJET-III and DPMJET II.55, as well as a harder proton primary spectrum parametrization could better account for the experimental observations. For charmed hadrons, this implementation of DPMJET-II in CORSIKA underestimates diffractive events. This is particularly evident for charmed baryons. In figure 7.2, the Z-moments and the multiplicities are shown for all energies and models. Z-moments show a similar trend to what is described for the energy fractions with a weight that takes into account the slope of the cosmic ray spectrum. It is also noticeable that the spread between models is much larger for kaons than for pions.

7.3.2 Extended Air Shower

7.3.2.1 lateral distribution function

Measurements of the lateral distribution of the penetrating muon component of extended air showers (EAS) underground are sensitive to the chemical composition of primaries, their energy and interaction characteristics. One critical component of these models is the forward production of pions and kaons in high-energy hadronic interactions. Most of the pions and kaons are produced at low transverse momentum. The validity of approaches suggested in [30] in which it is hypothesized that the high transverse momentum muons can be used to infer their production rate from heavy quarks is tested. For purposes of illustration the first interaction alone(no shower) is separated from the case of full shower formation for prompts and conventional muons, further proton showers are separated from iron showers to see the affect of heavier primaries. Lateral distribution function gives the average number of muons per metre square of area in the radial direction away from the point of reference. Lateral distribution functions are plotted for the different cases of full cosmic ray spectrum, full cosmic ray spectrum with zenith angle greater than 80 degrees, primaries in the energy range of 1-1000 PeV and primaries of fixed energy 1 PeV at zenith angle of 65 degrees. Most of the muons are produced along the direction of the shower core and decrease as we go away from the shower core as is reflected by the falling slope of these plots. Usually the number of muons from first interaction are lower than multiple interactions considering that multiple interaction encompasses first interaction. All these plots taken together prove a single important point that the strategy to separate prompt muons from conventional muons using lateral distribution functions does not look promising. One possible explanation is that the transverse and longitudinal momenta are on average larger for charmed secondaries as can be seen in figure 6.3 for the case of 1PeV fixed primaries at a zenith angle of 65 degrees therefore, the lateral distribution of muons at the surface measured from the shower axis is not much different for prompt muons than conventional ones neither after the first interaction nor after full shower development. The various trends can be read from figures section bearing in mind that at very large lateral distances generation statistics also play a role. These plots are shown in figures 7.4, 7.5, 7.6, 7.7, 7.8, 7.9.

7.3.2.2 Zenith Angle and Energy Spectra

Detailed studies of zenith angle and energy spectra is not the primary objective of this chapter. Testing of the DPMJET-II.55 model is done and distributions of surface energy, energy at detector and zenith angle are shown. As is known from [31] prompts exhibit a harder energy and zenith angle spectra and can be seen in figures 7.10, 7.11 and 7.12. It is hypothesized during my earlier analysis that the production of charmed particles in the forward direction would produce muons of multiplicity one and here we test that hypothesis using our simulation and see that is not the case.

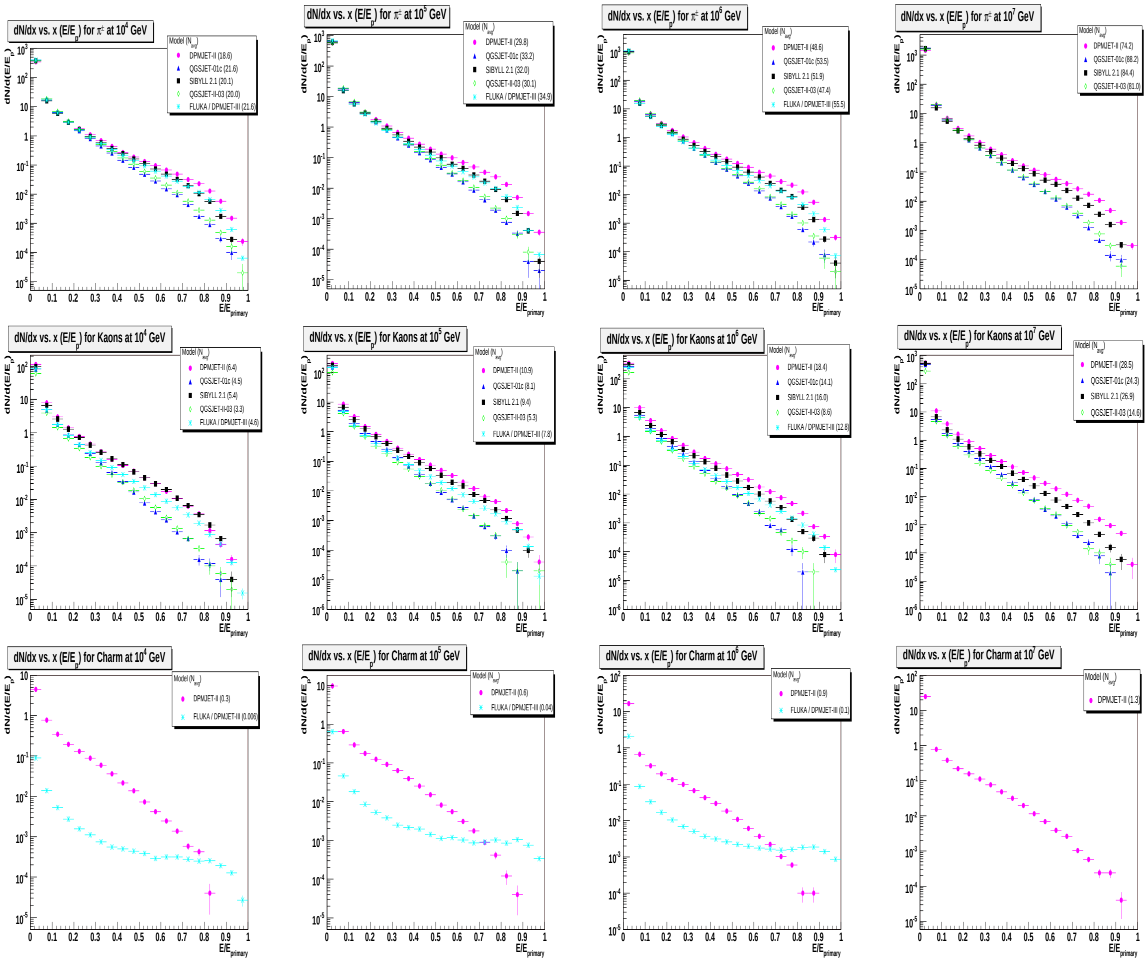

Figure 7.1: Energy fraction distributions using various models for charmed baryon and mesons for energies of 10, 10^2, 10^3, and 10^4 TeV

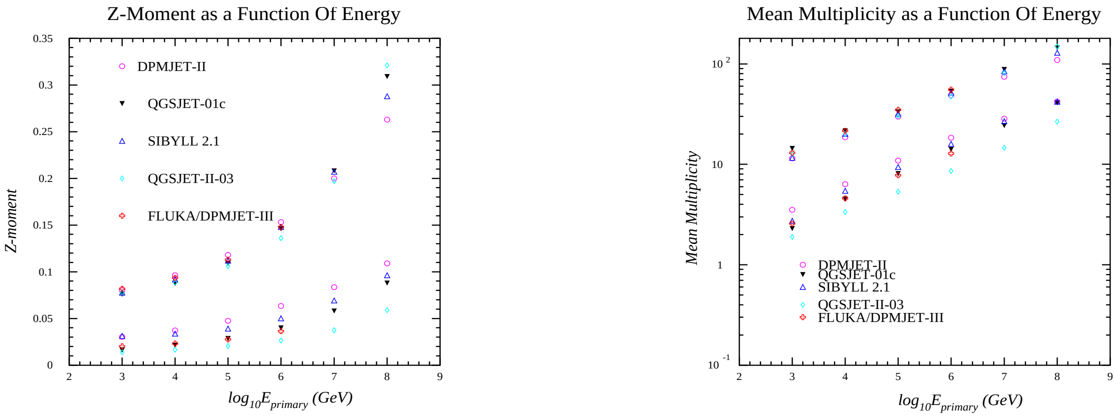

Figure 7.2: The mean multiplicity and the Z-moments of pions and kaons as a function of primary energy. The top ensemble of points denote pions while the bottom ones denote kaons

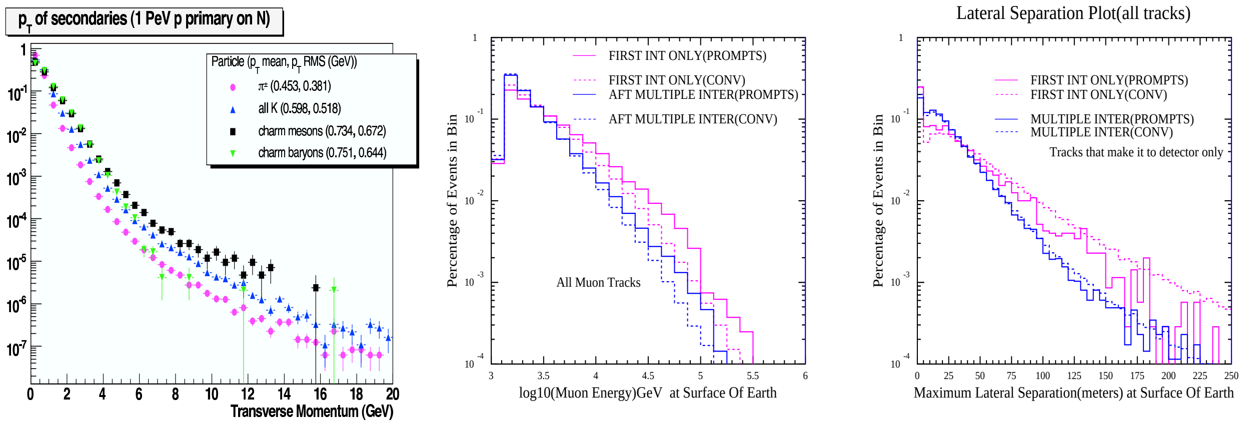

Figure 7.3: The trasverse momentum, longitudinal momentum and lateral separation of the secondary particles produced by air showers for a 1 PeV monoenergetic beam of primary protons at a fixed zenith angle of 65 degrees.

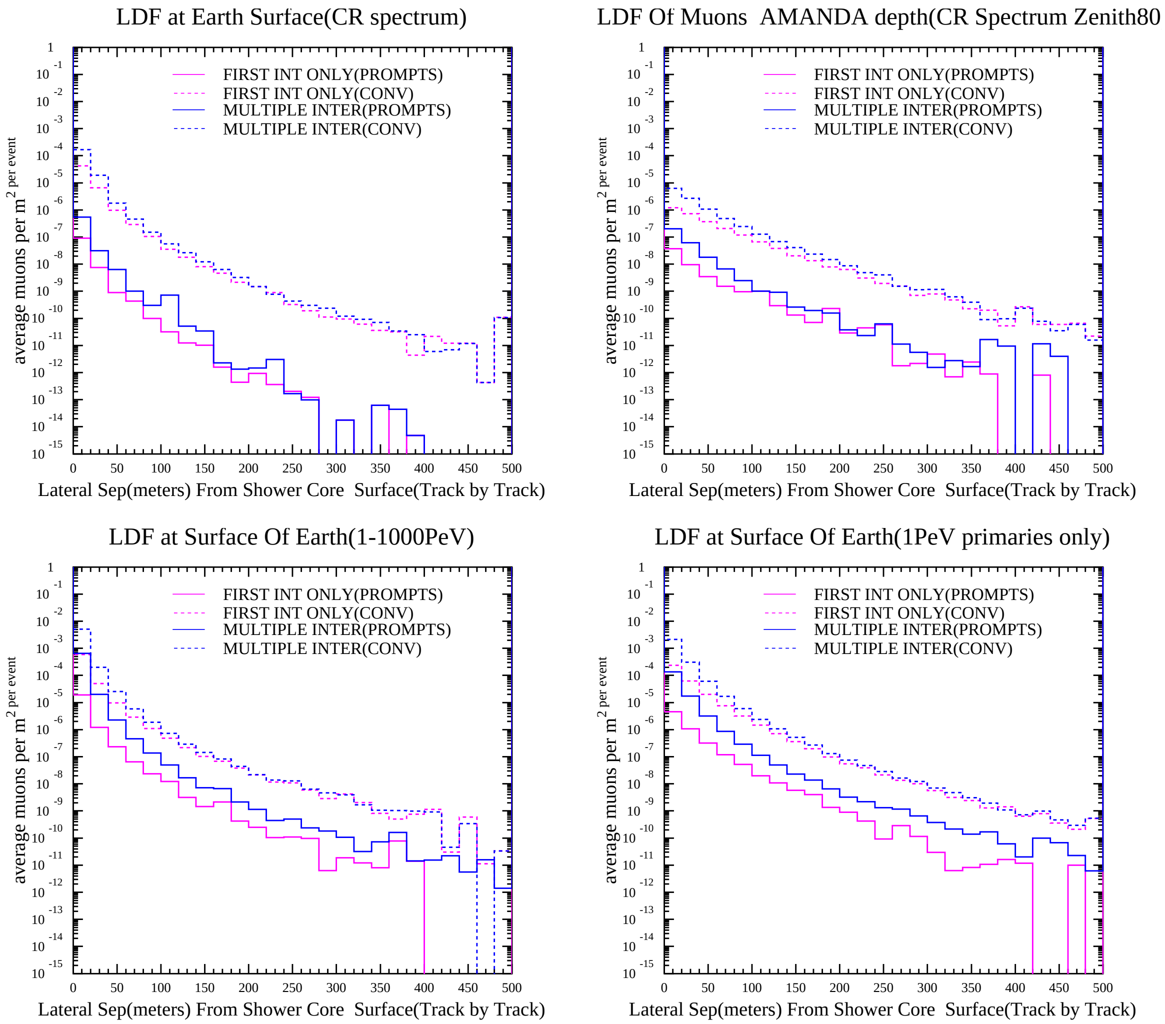

Figure 7.4: Shows the average number of muons produced per event as a function the lateral separation from the shower core at surface of earth for showers initiated by the full cosmic ray spectrum, full cosmic ray spectrum for zenith>80 degrees, for primaries in the energy range of 1-1000 PeV and monoenergetic primary energy of 1 PeV with no showering (only the first interaction) and after the full shower develops (multiple interactions) with events containing atleast 1 prompt muon (produced from a charmed particle) tagged as “PROMPTS” and for no prompt muon involved as “CONV”. All data has been normalized to 1 years worth lifetime

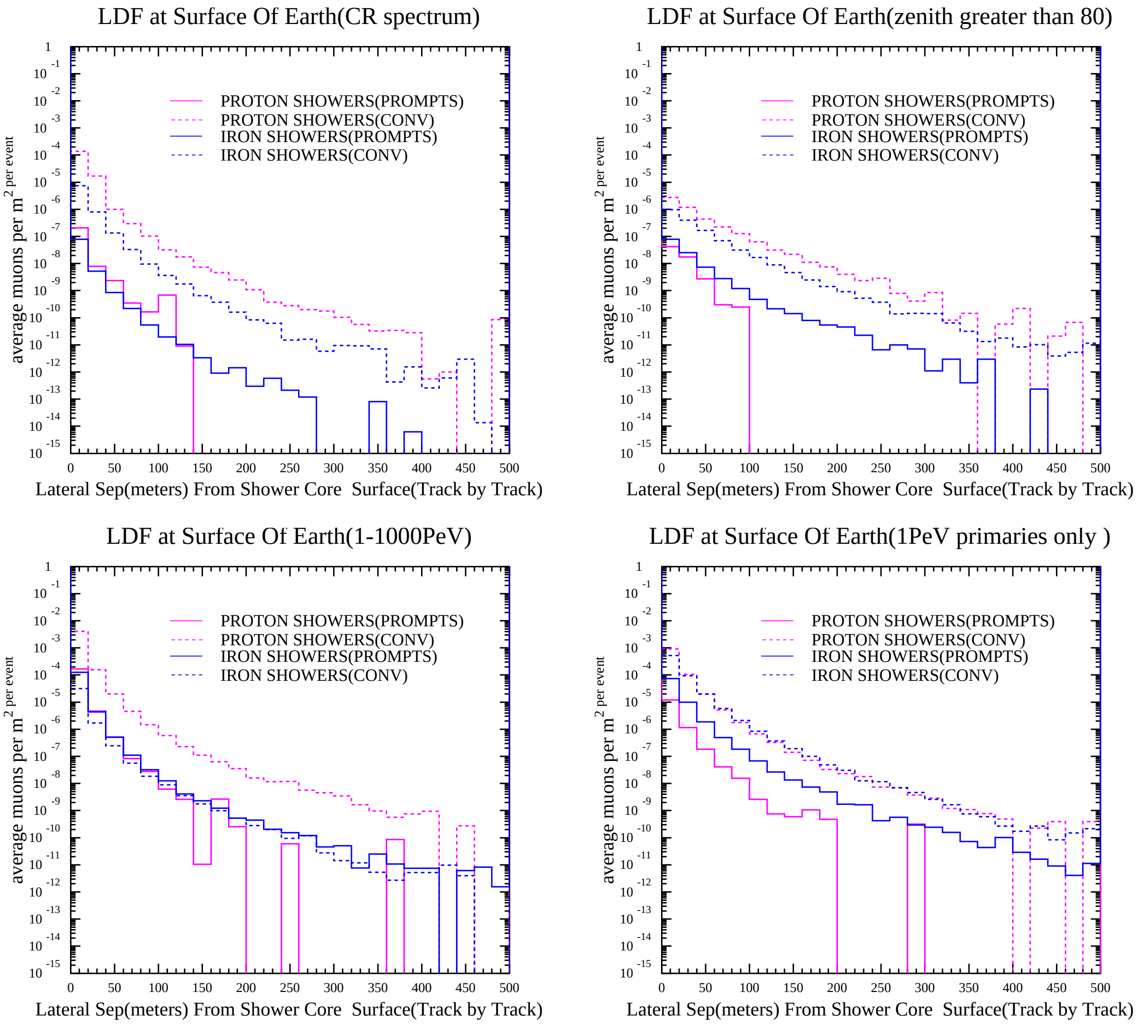
LDF at Surface Of Earth(CR spectrum)

LDF at Surface Of Earth(zenith greater than 80)

LDF at Surface Of Earth(1-1000PeV)

LDF at Surface Of Earth(1PeV primaries only)

Figure 7.5: Shows the average number of muons produced per event as a function the lateral separation from the shower core at surface of earth for showers initiated by the full cosmic ray spectrum, full cosmic ray spectrum for zenith>80 degrees, for primaries in the energy range of 1-1000 PeV and monoenergetic primary energy of 1 PeV after the full shower develops (multiple interactions) with showers produced by protons and iron identified separately. All data has been normalized to 1 years worth lifetime

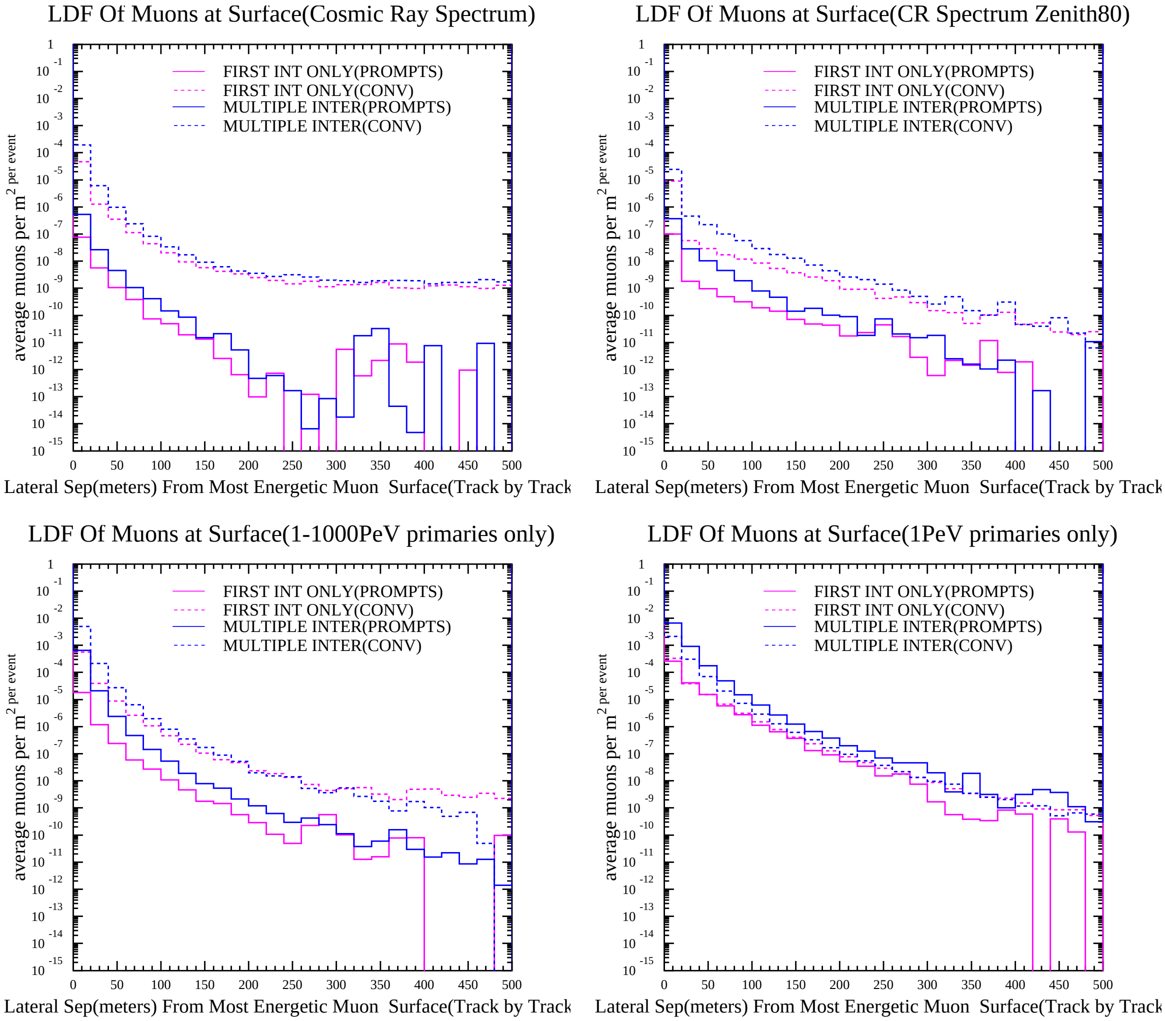

Figure 7.6: Shows the average number of muons produced per event as a function the lateral separation from the most energetic muon at surface of earth for showers initiated by the full cosmic ray spectrum, full cosmic ray spectrum for zenith>80 degrees, for primaries in the energy range of 1-1000 PeV and monoenergetic primary energy of 1 PeV with no showering (only the first interaction) and after the full shower develops (multiple interactions) withevents containing atleast 1 prompt muon (produced from a charmed particle) tagged as “PROMPTS” and for no prompt muon involved as “CONV”. All data is normalized to 1 years worth lifetime

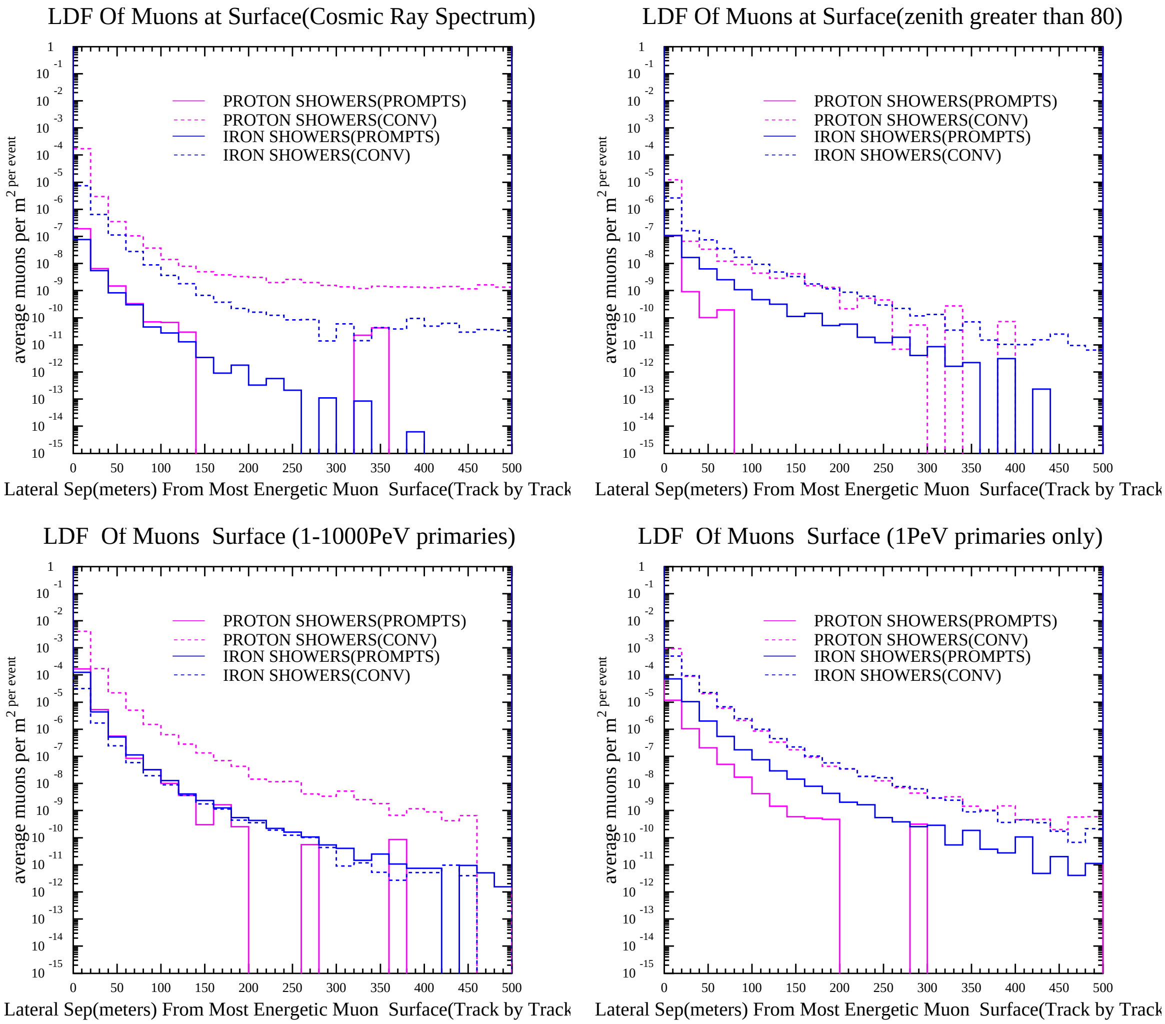

Figure 7.7: Shows the average number of muons produced per event as a function the lateral separation from the most energetic muon at surface of earth for showers initiated by the full cosmic ray spectrum, full cosmic ray spectrum for zenith>80 degrees, for primaries in the energy range of 1-1000 PeV and monoenergetic primary energy of 1 PeV after the full shower develops (multiple interactions) with showers produced by protons and iron identified separately. All data is normalized to 1 years worth lifetime

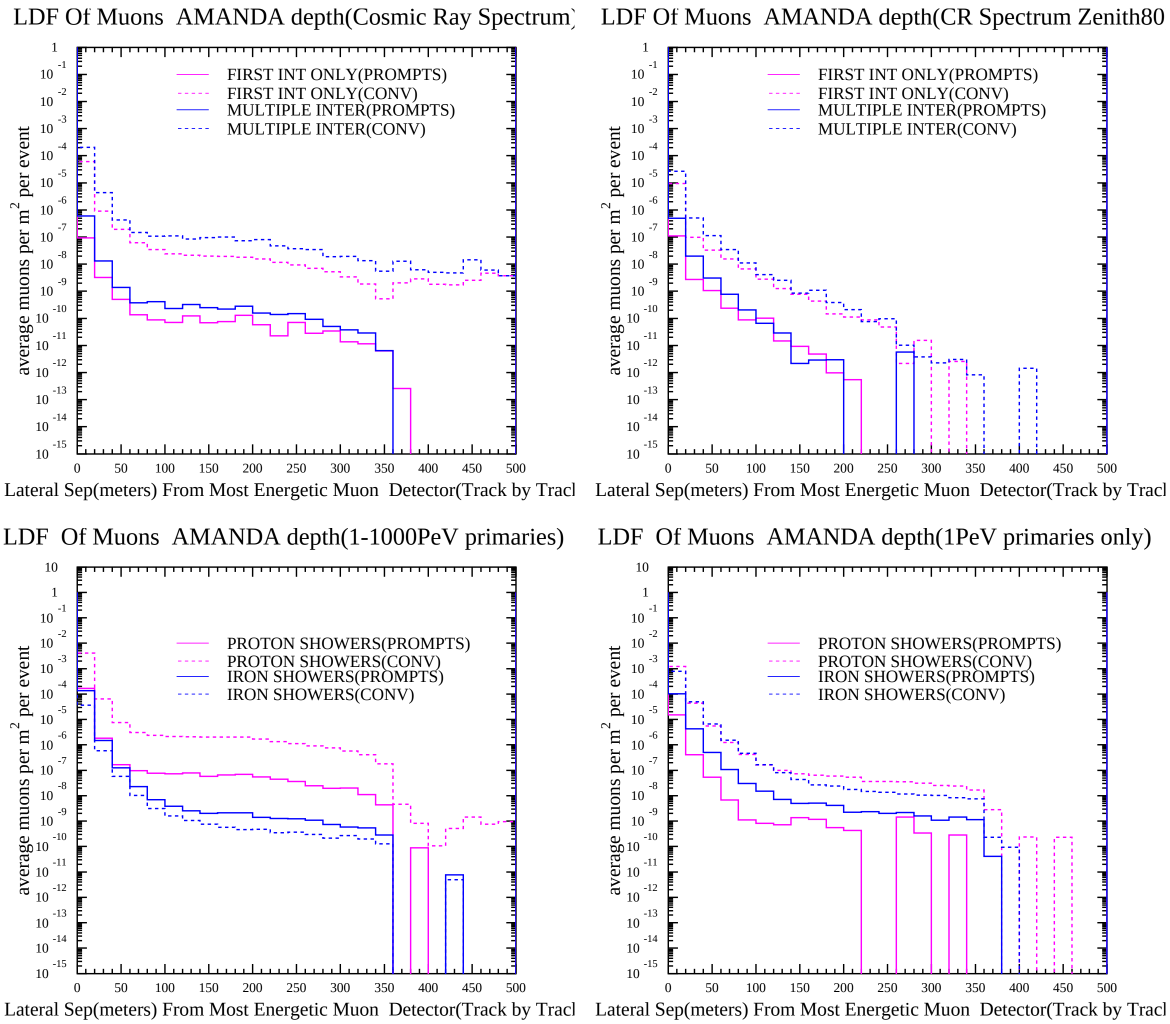

Figure 7.8: Shows the average number of muons produced per event as a function the lateral separation from the most energetic muon at detector for showers initiated by the full cosmic ray spectrum, full cosmic ray spectrum for zenith>80 degrees, for primaries in the energy range of 1-1000 PeV and monoenergetic primary energy of 1 PeV with no showering (only the first interaction) and after the full shower develops (multiple interactions) with events containing atleast 1 prompt muon (produced from a charmed particle) tagged as "PROMPTS" and for no prompt muon involved as "CONV". All data is normalized to 1 years worth lifetime

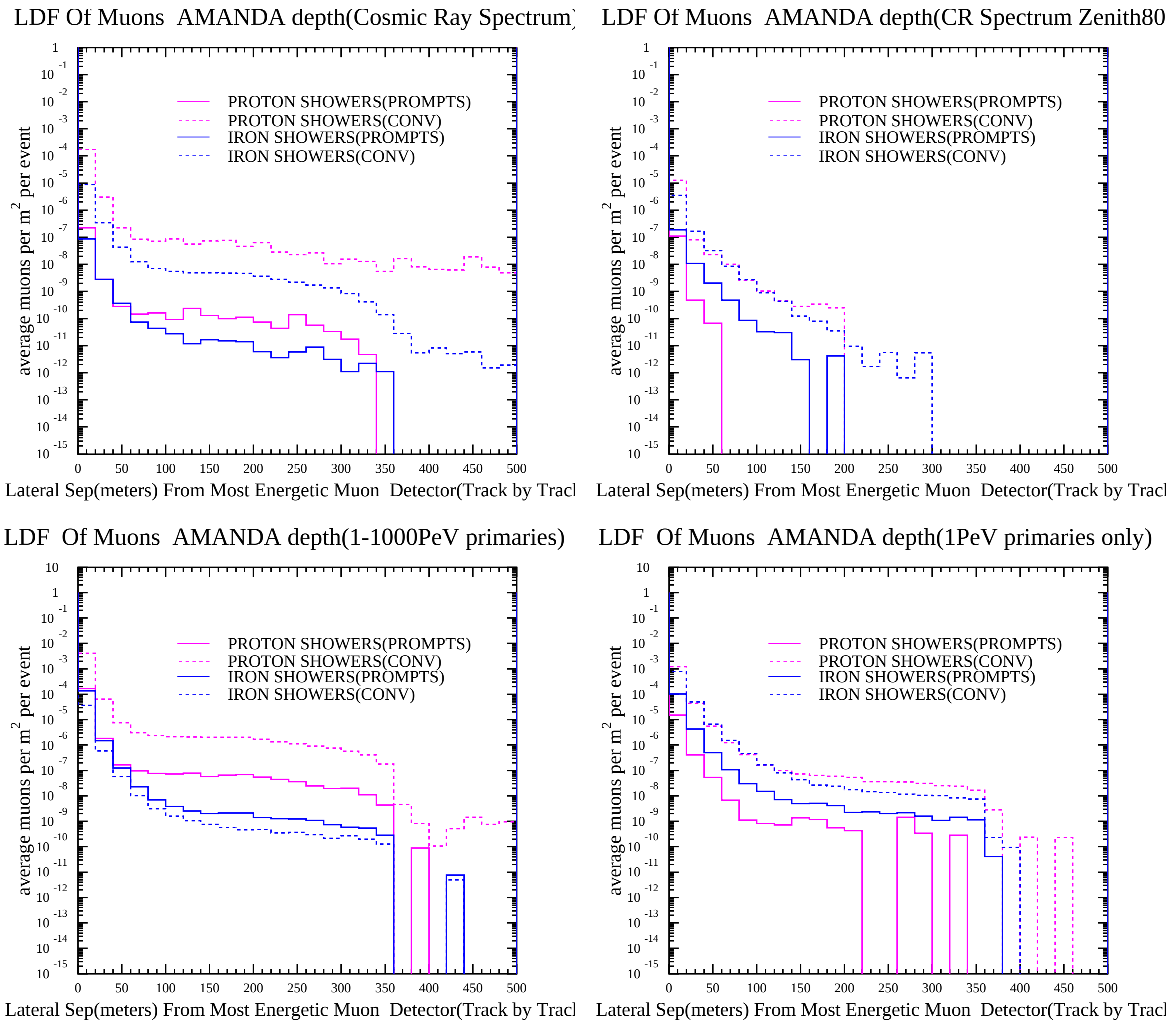

Figure 7.9: Shows the average number of muons produced per event as a function the lateral separation from the most energetic muon at detector for showers initiated by the full cosmic ray spectrum, full cosmic ray spectrum for zenith>80 degrees, for primaries in the energy range of 1-1000 PeV and monoenergetic primary energy of 1 PeV after the full shower develops (multiple interactions) with showers produced by protons and iron identified separately. All data is normalized to 1 years worth lifetime

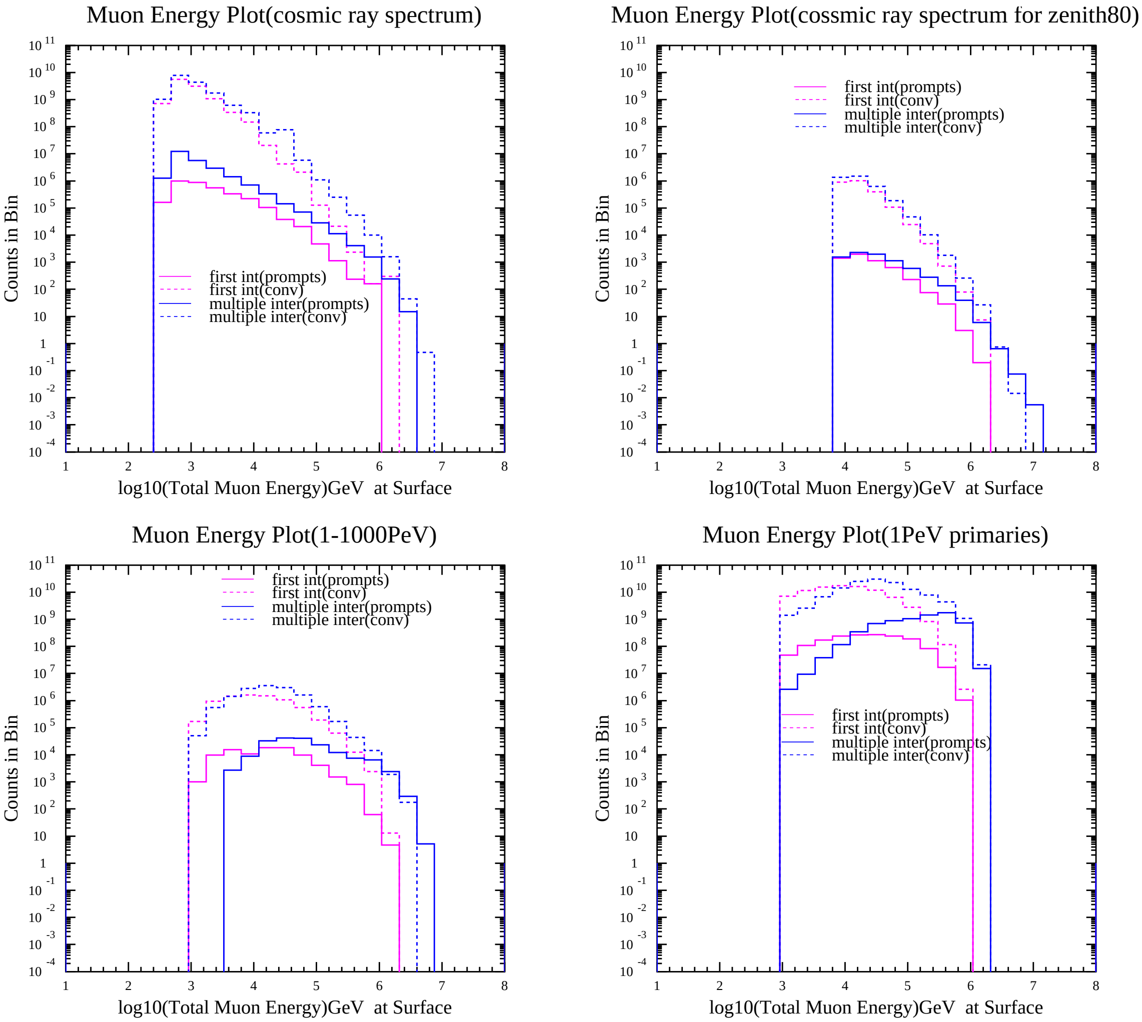

Figure 7.10: Shows the sum total of surface energy of all the muons in an event for showers initiated by the full cosmic ray spectrum, full cosmic ray spectrum for zenith>80 degrees, for primaries in the energy range of 1-1000 PeV and monoenergetic primary energy of 1 PeV with no showering (only the first interaction) and after the full shower develops (multiple interactions) with events containing atleast 1 prompt muon (produced from a charmed particle) tagged as “PROMPTS” and for no prompt muon involved as “CONV”. All data is normalized to 1 years worth lifetime

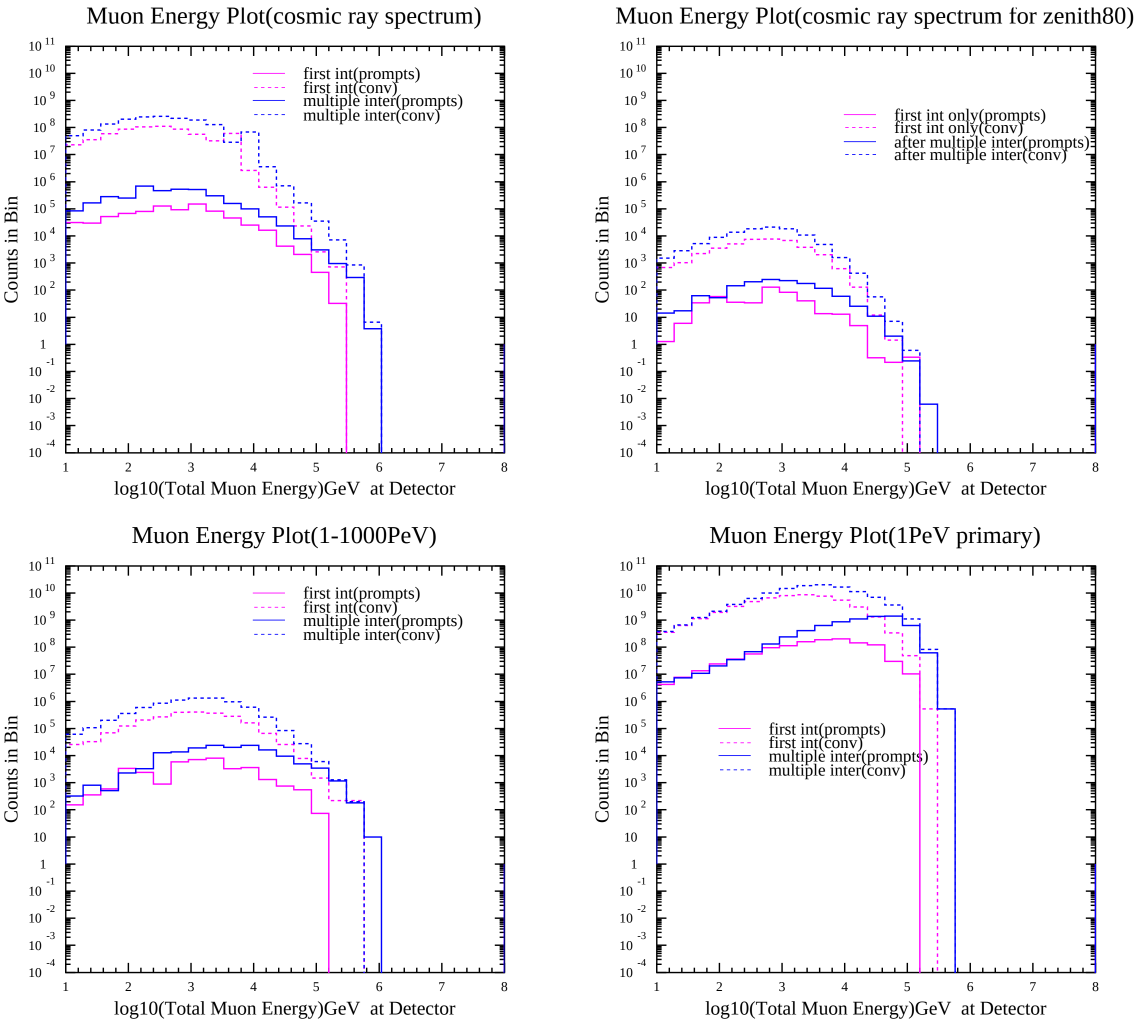
Muon Energy Plot(cosmic ray spectrum)

Muon Energy Plot(cosmic ray spectrum for zenith80)

Muon Energy Plot(1-1000PeV)

Muon Energy Plot(1PeV primary)

Figure 7.11: Shows the sum total of energy of all the muons in an event at the detector for showers initiated by the full cosmic ray spectrum, full cosmic ray spectrum for zenith>80 degrees, for primaries in the energy range of 1-1000 PeV and monoenergetic primary energy of 1 PeV with no showering (only the first interaction) after the full shower develops (multiple interactions) with events containing atleast one prompt muon (produced from a charmed particle) tagged as “PROMPTS” and for no prompt muon involved as “CONV”. All data is normalized to 1 years worth lifetime

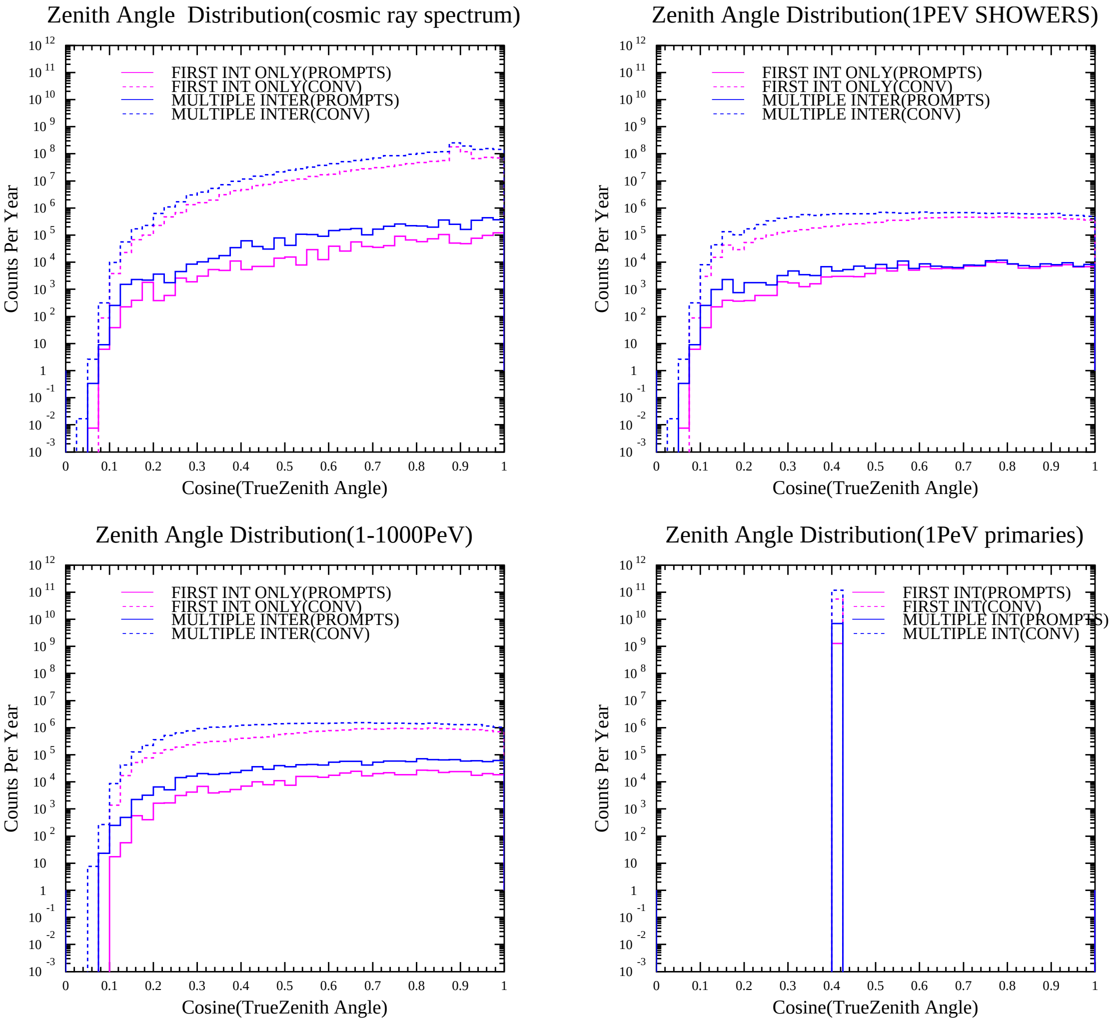

Zenith Angle Distribution(cosmic ray spectrum)

Zenith Angle Distribution(1PEV SHOWERS)

Zenith Angle Distribution(1-1000PeV)

Zenith Angle Distribution(1PeV primaries)

Figure 7.12: Shows the zenith angle distribution of showers initiated by the full cosmic ray spectrum, full cosmic ray spectrum for zenith>80 degrees, for primaries in the energy range of 1-1000 PeV and monoenergetic primary energy of 1 PeV with no showering (only the first interaction) and after the full shower develops (multiple interactions) with events containing atleast 1 prompt muon (produced from a charmed particle) tagged as "PROMPTS" and for no prompt muon involved as "CONV". All data is normalized to 1 years worth lifetime

Chapter 8

Results and Conclusions

8.1 Shape Analysis

In a usual AMANDA analysis, confidence intervals are constructed based on the number of events in the final data sample after taking into account the predicted background and signal events. Statistical and systematic uncertainities are incorporated into the confidence interval based on the work of Feldman and Cousin [7]. These cut and count methods do not consider shape information about the predicted or observed spectrum of events. This analysis will compare the shape and normalization of the observed data to simulations based on the model for background and signal flux. The number of optical modules fired is a powerful variable used in this analysis. By using shape and normalization information for optical modules fired it is hoped that the atmospheric muon background can be better understood and limits could be placed on prompt atmospheric muon models.

8.2 Simulation and Fitting Procedure

The simulation for the signal (prompt muon) is done using the DPMJET model while the background (conventional muon) was done using SYBILL. Two ice models AHA and Millenium were simulated. The AHA model is flatter compared with the Millenium [10]. While the Millenium model is simulated both for the background and signal, the AHA model is simulated only for the background and the simulation for AHA signal is obtained by appropriate scaling. It is the tradition of most AMANDA related analysis to use the hybrid frequentist-Bayesian method based on the work of Cousins and Highland [8] to construct a confidence belt for the signal. The nature of downgoing muon analysis presents the challenge of dealing with unclear systematic uncertainities at high energies so in this analysis we use slope fitting of the background and signal to the experimental data to determine limits on the assumed signal spectra.

8.3 Fitting Procedure

The number of channel hit spectra at the final stage (after all the cuts) for the experimental data is fitted using the simulated background and signal (assuming there is no preference for the AHA or the Millenium model). The scaling parameters for the simulated background and the signal for the Millenium model are denoted by $f_{\mathrm{C-MIL}}$ and f_{PROMPT} respectively and $f_{\mathrm{C-AHA}}$ to denote AHA background and these are parameters are fitted using a chisquare based approach. The AHA signal was not simulated but was scaled using the fitted background ratio of the two models. The idea of slope fitting would be to minimize the chisquare while fitting these parameters with the experimental data. For purposes of this minimization only bins numbered

6 to 17 (number of optical modules fired greater than 180) are used as it would be more representative of the high-energy response of the detector. The best fit values of $f_{\mathrm{C-MIL}}$, f_{PROMPT}, $f_{\mathrm{C-AHA}}$ are obtained by minimizing the chisquare and confidence bands on the scaling of the signal are constructed. In figure 8.1 the best chisquare is shown at different allowed levels of signal. Error contours for the fraction of allowed AHA and Millenium background forcing signal to be zero (demonstrative purposes) and the best fit value of signal and the 90% level for signal contribution are also shown in figures 8.2, 8.3 and 8.4 respectively. The spectra before scaling and after scaling for the best fit values are shown in figures 8.5 and 8.6 respectively. Fitting equations and scaling parameters fitted for are described by the below equations.

$$\chi^2 = \sum_{\mathrm{bins}} \frac{(N_i^{\mathrm{DATA}} - N_i^{\mathrm{PRED}})^2}{\sigma_i^2} \tag{8.1}$$

$$\begin{aligned} N_i^{\mathrm{PRED}} &= f_{\mathrm{C-AHA}} N_{i\mathrm{C-AHA}}^{\mathrm{PRED}} + f_{\mathrm{C-MIL}} N_{i\mathrm{C-MIL}}^{\mathrm{PRED}} \\ &+ f_{\mathrm{PROMPT}} \left\{ N_{i\mathrm{P-MIL}}^{\mathrm{PRED}} + \frac{f_{\mathrm{C-AHA}}}{f_{\mathrm{C-MIL}}} N_{i\mathrm{P-AHA}}^{\mathrm{PRED}} \right\} \end{aligned} \tag{8.2}$$

N_i^{DATA} is observed experimental data counts in each bin. N_i^{PRED} is predicted simulation data counts in each bin. σ_i^2 is the variance given by ROOT after reweighting. $f_{\mathrm{C-AHA}}$ is the unknown scale factor for Conventional muon background using AHA model. $f_{\mathrm{C-MIL}}$ is the unknown scale factor for conventional muon background using Millenium model. f_{PROMPT} is the unknown scale factor for prompt muon signal using the Millenium model. $N_{i\mathrm{C-AHA}}^{\mathrm{PRED}}$ is the predicted conventional background using AHA model. $N_{i\mathrm{C-MIL}}^{\mathrm{PRED}}$ is the predicted conventional background using the Millenium model. $N^{\text{PRED}}_{i\text{P}-\text{MIL}}$ is the predicted prompt signal using the Millenium model. $N^{\text{PRED}}_{i\text{P}-\text{AHA}}$ is the predicted prompt signal using the AHA model.

8.4 Prompt Atmospheric Neutrino Upper limits

Since prompt muons have a harder (less steep) spectrum than the conventional atmospheric neutrinos, it is possible to search for a prompt neutrino flux by separating the two event classes in energy. A limit on prompt muons is equivalent to a limit of prompt neutrinos [31]. The Naumov RQPM model is a non-perturbative model of prompt atmospheric neutrinos and incorporates data from primary cosmic ray and hadronic interaction experiments. The upper limit of this model at 90% confidence level using shape based spectral fitting is $3.67{\cdot}\Phi_{\text{RQPM}}$.

8.5 Discussion for Better Analysis in Future

The biggest problem that makes this analysis tricky is the fact that we don't have a good model for prompt muon production and DPMJET-II.55, far from being accurate is the best we could get to use in conjunction with SYBILL conventional muon Monte Carlo. Events containing one or more muons whose parent is a charmed particle were tagged as prompt muons and the experimental data was fitted to incorporate this component to minimize the chisquare and this was used to derive an upper limit on the charm cross-section. This approach suffers from the fact that the prompt muon event production rate the way it is defined is not linear with an increase in charm cross-section and hence placing upper limits this way is far from the correct way of doing it. A correct approach would be to change the charm cross-section up and down and produce muon event rates for the prompt muon signal and construct the chisquare surface for the fit to the experimental data and derive upper limits on the cross section based on it.

Further another issue in this analysis is that the SYBILL conventional Monte Carlo doesn't produce any charmed particles and this is used in combination with a signal simulation of DPMJET that samples charmed particles from the charm cross-section, these are not two mutually exclusive sets when added up to compare to the experimental data and is a rough approximation to derive upper-limits on the signal.

8.6 Conclusion

This analysis placed an upper limit on the prompt neutrino model of RQPM using prompt muon analysis and set a constraint on the model. This result is the first of its kind in using a downgoing muon analysis to set an upper limit on the prompt neutrinos. AMANDA-II has now been integrated into IceCube. The main aim of IceCube is to detect extra-terrestrial neutrinos and the level of uncertainty on the prompt neutrino flux is of great interest in calculating the sensitivity of IceCube experiment to extra-terrastrial neutrinos. Using a downgoing muon analysis we constrain the RQPM model to a factor of 3.67 at 90% confidence.

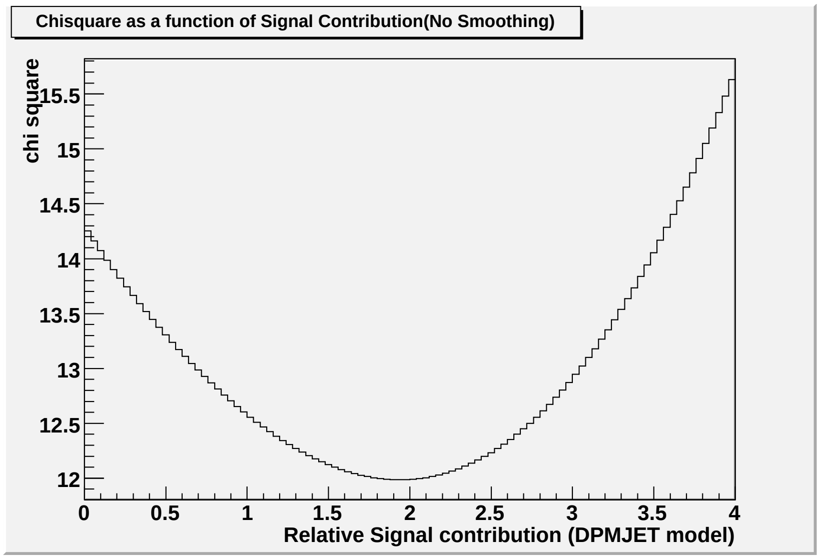

Figure 8.1: The minimized value of chisquare is shown for different levels of signal.

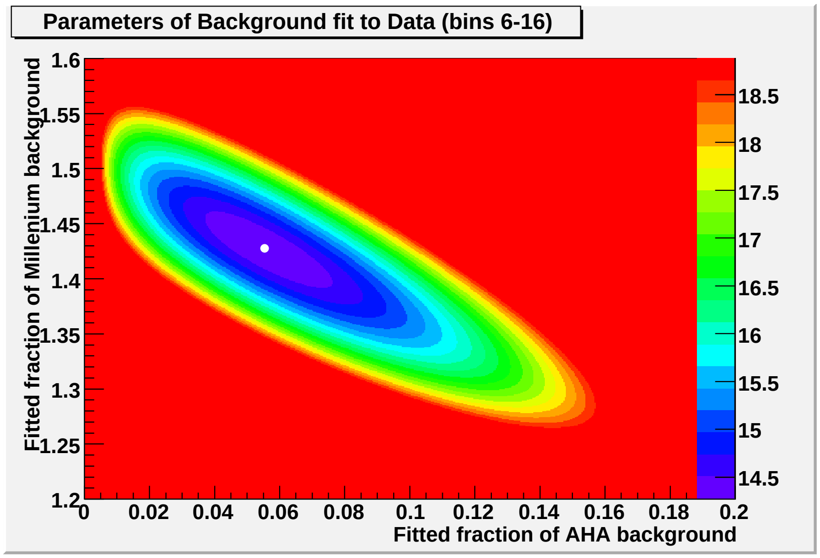

Figure 8.2: The elliptical contours of chisquare for the fraction of Millenium and AHA backgrounds are shown forcing the signal contribution to be zero while making a fit to the data.

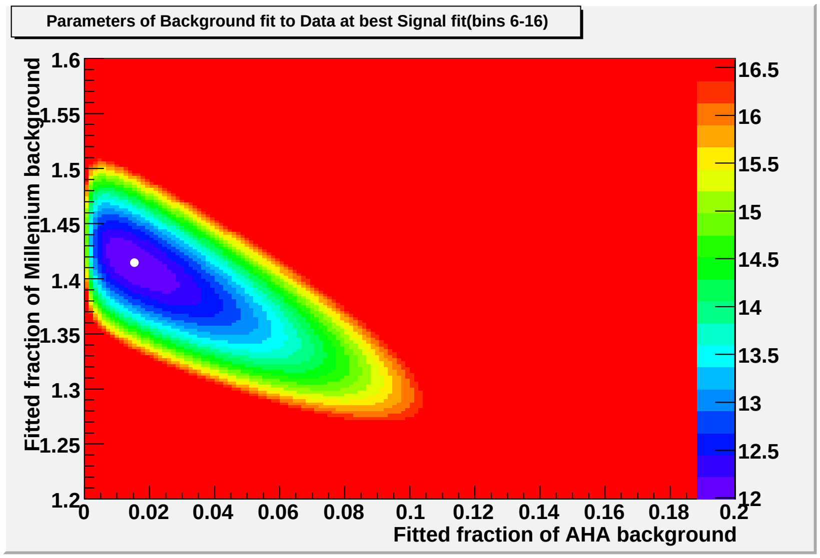

Figure 8.3: The elliptical contours of chisquare for the fraction of Millenium and AHA backgrounds are shown for best fit value of signal while making a fit to the data.

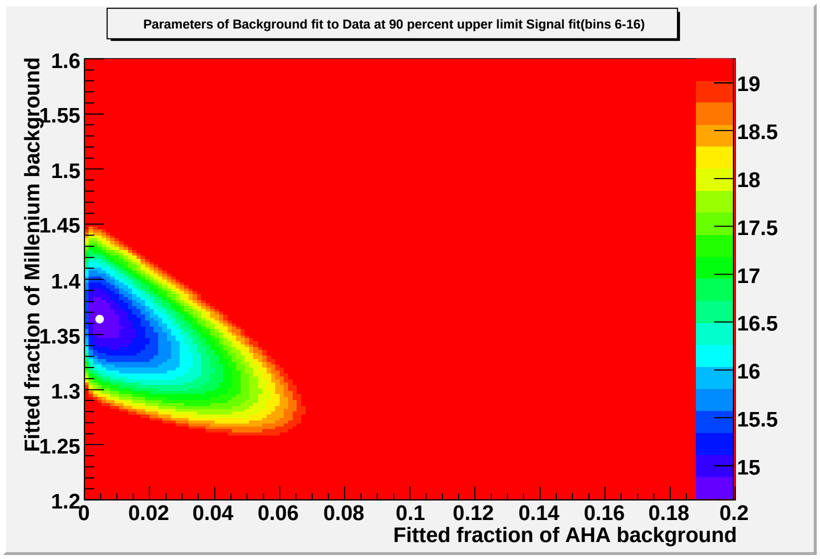

Figure 8.4: The elliptical contours of chisquare for the fraction of Millenium and AHA backgrounds are shown for the allowed level of signal at 90% confidence level while making a fit to the data.

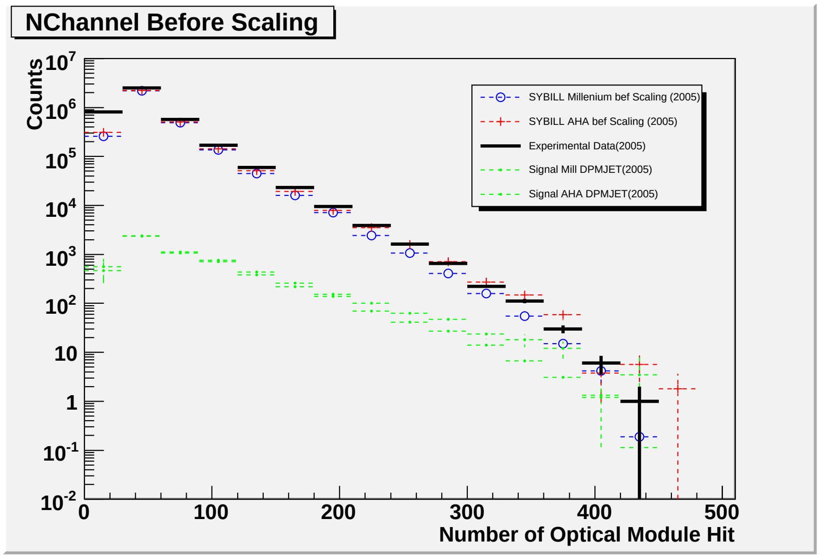

Figure 8.5: The signal and background spectra for the AHA and Millenium models together with the minimum bias experimental data before fitting are shown.

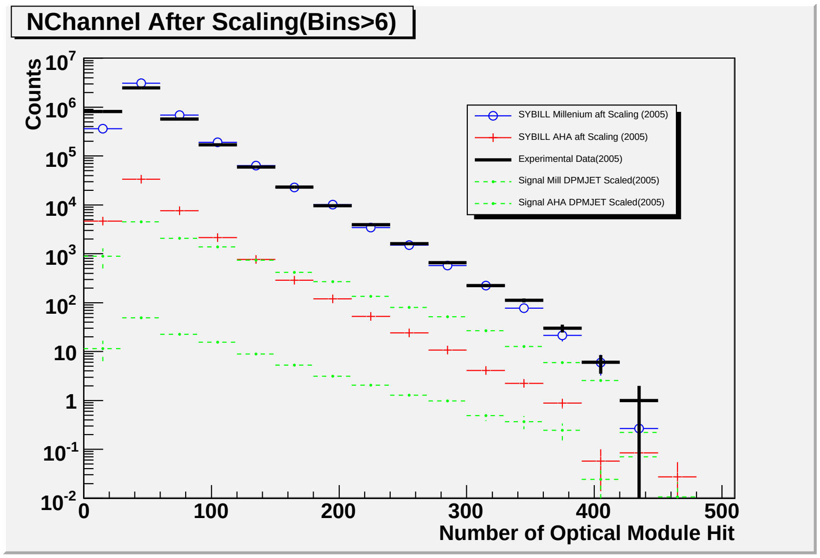

Figure 8.6: The scaled levels at the best fit values of signal and background spectra for the AHA and Millenium models are shown together with the minimum bias experimental data.

Bibliography

[1] Jim Green, private communication.

[2] C.G.S. Costa, Astropart. Phys. **16**, 193 (2001).

[3] G. Fiorentini, A. Naumov, and F.L. Villante, Phys. Lett. B **510**, 173 (2001).

[4] G. Gelmini, P. Gondolo and G. Varieschi *Measuring the prompt atmospheric neutrino flux with down-going muons in neutrino telescopes* , Jan 2003 Phys. Rev. D 67, 017301.

[5] E.V. Bugaev *et al.*, Il Nuovo Cimento **12C**, No. 1, 41 (1989).

[6] E.V. Bugaev *et al.*, Phys. Rev. D **58**, 054001 (1998).

[7] Ochs, Nucl. Phys. B118, 397 (1977).

[8] E. V. Bugaev, A. Misaki, V. A. Naumov, T. S. Sinegovskaya, S. I. Sinegovsky, and N. Takahashi *Atmospheric muon flux at sea level,underground and under-water*, Phys. Rev. D 58, 054001 (1998), Issue 5, September 1998.

[9] Athina Meli, private communication.

[10] D. Heck, J. Knapp, J.N. Capdevielle, G. Schatz, and T. Thouw,Tech. Rep. FZKA 6019, Forschungszentrum Karlsruhe (1998).

[11] http://www.icecube.wisc.edu/ boersma/filter2005/webpage/index.html.

[12] D. Pandel, Diploma Thesis, Humboldt-Universität zu Berlin, Berlin, Germany, February 1996.

[13] http://www.icecube.wisc.edu/ jkelley/simulation/dcorsweighting.pdf.

[14] http://www.icecube.wisc.edu/ jkelley/simulation/livetimes.pdf.

[15] J. Horandel, *Astropart.Phys.*, 19(2003) 193.

[16] http://www.icecube.wisc.edu/ jkelley/simulation/aha/aha.html.

[17] H. Kampert, Nuclear Physics B (Proc. Suppl.), 165 (2007).

[18] J. Ahrens *et al.*, Phys. Rev. Lett. **90**, 251101 (2003).

[19] P. Desiati *et al.*, *Response of AMANDA-II to Cosmic Ray Muons*,Proc. of 28th ICRC, Hamburg, Germany (2003).

[20] D. Heck, T. Pierog, J. Knapp, *CORSIKA: an air shower simulation program*: http://www-ik.fzk.de/corsika/.

[21] http://www.fluka.org; A. Fassò, A. Ferrari, J. Ranft and P.R. Sala, *FLUKA: a multi-particle transport code*,CERN-2005-10 (2005), INFN/T C_05/11, SLAC-R-773;A. Fassoò *et al.* , *The physics models of FLUKA: status and recent developments*, Computing in High Energy and Nuclear Physics 2003 Conference (CHEP2003), La Jolla, CA, USA, March 24-28, 2003, (paper MOMT005), eConf C0303241 (2003), [arXiv:hep-ph/0306267].

[22] Spencer Klein, *Studying High pT Muons in Cosmic-Ray Air Showers*,2 Dec 2006 [arXiv:stro-ph/0612051 v1].

[23] N.N. Kalmykov *et al.*, Nucl. Phys. **B** (Proc. Suppl.) **52B** (1997) 17.

[24] S. Ostapchenko, Nucl. Phys. **B** (Proc. Suppl.) **151** (2006) 143 [arXiv:hep-ph/0412332].

[25] R.S. Fletcher *et al.*, Phys. Rev. **D50** (1994) 5710.

[26] T. Sjostrand *A brief introduction to PYTHIA 8.080.*

[27] G.J. Feldman and R.D. Cousins *Unified approach to the classical statistical analysis of small signals* , Phys. Rev. D 57, 3873-3889 (1998).

[28] R.D. Cousins amd V.L. Highland *Incorporating systematic uncertainties into an upper limit* , Nucl. Ins. Meth. Phys. Res. A32 0 331 (1992).